

3807

NASA CR - 195322



Development and Verification of a Model to Predict
Impingement Currents for Ion Thrusters

Prepared for

LEWIS RESEARCH CENTER

IONAL AERONAUTICS AND SPACE ADMINISTRATION

Grant NAG3-1206

by

Jeffery M. Monheiser

April 1994

Approved by

Paul J. Wilbur
Department of Mechanical Engineering
Colorado State University
Fort Collins, Colorado 80523

N94-29546

Unclass

G3/20 0003807

(NASA-CR-195322) DEVELOPMENT AND
VERIFICATION OF A MODEL TO PREDICT
IMPINGEMENT CURRENTS FOR ION
THRUSTERS (Colorado State Univ.)
101 p

1. Report No. NASA CR-195322 E-8756		2. Government Accession No.		3. Recipient's Catalog No.	
4. Title and Subtitle Development and Verification of a Model to Predict Impingement Currents for Ion Thrusters				5. Report Date April 1994	
				6. Performing Organization Code	
7. Author(s) Jeffery M. Monheiser				8. Performing Organization Report No.	
				10. Work Unit No.	
9. Performing Organization Name and Address Department of Mechanical Engineering Colorado State University Fort Collins, CO 80523				11. Contract or Grant No. NAG3-1206	
				13. Type of Report and Period Covered	
12. Sponsoring Agency Name and Address National Aeronautics and Space Administration Washington, D.C. 20564				14. Sponsoring Agency Code	
15. Supplementary Notes Grant Monitor - Vincent K. Rawlin, NASA Lewis Research Center, Cleveland, OH 44135 This report is a reproduction of the Ph. D. dissertation of Jeff Monheiser. It is submitted to the sponsor and the distribution list in this form as a presentation of the technical material and as an indication of the academic program sponsored by the grant.					
16. Abstract <p>A 1-D model describing the production of ions that impinge on accelerator grids and cause them to erode is developed. Experimental data are obtained that show measured impingement currents agree with currents computed using this model to within $\pm 30\%$. Data are also presented which show that impingement-current ions are produced by charge-exchange rather than single or multi-step, electron-impact reactions. Electrical potentials measured in the regions adjacent to and downstream of an accel grid are presented to show that charge-exchange ions that impinge on the accel grid can be conveniently separated into two groups, one created upstream and the second created downstream of an ion-beam neutralization boundary. All of the ions created in the first region impinge on accel grids while only a fraction of those created downstream of the neutralization boundary do. Data are also presented to show that experimentally measured values of the distance from the accel grid to this neutralization boundary agree with values computed using an equation developed by Kerslake.</p> <p>The 1-D model can be used to separate the relative contributions to impingement current ions produced from background atoms and atoms that come from the thruster. The model is applied to show that ions produced from xenon background atoms dominate impingement currents measured in many ground tests. Impingement currents in space should be substantially less because this contribution to the current will be negligible.</p>					
17. Key Words (Suggested by Author(s)) Electrostatic Ion Thruster Impingement Current Charge-Exchange Ions			18. Distribution Statement Unclassified-Unlimited		
19. Security Classif. (of this report) Unclassified		20. Security Classif. (of this page) Unclassified		21. No of pages 94	
				22. Price*	

Table of Contents

List of Tables	vii
List of Figures	viii
I. Introduction	1
II. Theoretical Development of a One-Dimensional Impingement Current Model . .	7
A. Impingement Ion Production Mechanisms	7
B. One-Dimensional Impingement-Ion-Production Model	13
C. An Order-of-Magnitude Comparison between the Impingement Current Fractions Created by Charge-Exchange and Electron-Impact Ionization	17
D. An Approximation of the Neutral Density Profile	19
E. Evaluation of the Differential-Impingement-Current Integral	25
F. Simplification of the Comparison Between Theoretical and Experimental Measurements for the Length of Region Three	28
III. Experimental Apparatus and Procedure	30
IV. Experimental Results	38
A. Verification of The Dominance of Charge-Exchange Ion Production . .	38
B. Determination of the Differential-Impingement-Current-Integral Limits	44
C. Neutralization-Length Measurements	51
D. A Comparison Between Experimental and Computed Impingement Currents	65
V. Conclusions	80
VI. References	83
VII. Appendix A: Interpretation of Hot-Filament-Emissive Probe Floating Potential Data Obtained Within an Ion Beamlet	86

List of Tables

Table #	Title	Page #
1	Summary of Grid-Set Parameters	37

List of Figures

Figure #	Title	Page
1	Sketch of a Typical Ion Thruster	2
2	Ion Beamlet Definitions a) Physical Diagram of Ion Beamlet Formation b) Corresponding Centerline Potential Profile	8
3	Accel-Grid-View-Factor Definition	12
4	Monte-Carlo Simulation Geometry	21
5	Monte-Carlo Simulation Results and the Corresponding Exponential Curve Fit	23
6	Electrical Schematic	31
7	Mechanical Schematic of the Experimental Apparatus	33
8	Emissive and Langmuir Probe Schematics a) Hot-Filament, Bent, Emissive Probe b) Spherical Langmuir Probe	34
9	Background-Atom-Density Effects on Impingement Current a) Xe Propellant, Ar Backfill b) Ar Propellant, Xe Backfill	40
10	Effects of Neutralizer Bias Voltage on Maxwellian Electron Temperature and Impingement Current a) Maxwellian Electron Temperature b) Impingement Current	43
11	Typical Centerline Potential Profile	45

Figure #	Title	Page
12	Typical, Downstream, Equi-potential Surface Map for the 7-hole, 1-cm Grid Set	47
13	Typical, Downstream, Equi-Potential Surface Map for the 15-cm SHAG set	50
14	A Comparison of Inflection-Point and Floating-Potential Data	53
15	Effects of Beam Current on ℓ_n	54
16	Effects of Screen-Grid Potential on ℓ_n	56
17	Effects of Accel-Grid Potential on ℓ_n	57
18	Effects of Background-Atom Density on ℓ_n	58
19	Effects of Neutralizer-Bias Voltage on ℓ_n	60
20	Effects of Neutralizer-Keeper Current on ℓ_n	61
21	Comparison of $\tilde{\ell}_n$ Data Obtained on the 7-hole-Grid and SHAG Sets	63
22	A Comparison Between Measured and Predicted Effects on Changes in the Screen-Grid Potential	64
23	A Comparison Between Measured and Predicted Effects on Changes in the Accel-Grid Potential	66
24	Effects of Beam Current on Impingement Current for the 7-hole, 1/2-cm Grid Set	67
25	Effects of Screen-Grid Potential on Impingement Current for the 7-hole, 1/2-cm Grid Set	69
26	Effects of Accel-Grid Potential on Impingement Current for the 7-hole, 1/2-cm Grid Set	70
27	Effects of Background-Atom Density on Impingement Current for the 7-hole, 1/2-cm Grid Set	72

Figure #	Title	Page
28	Effects of Beam Current on Impingement Current for the 7-hole, 1-cm Grid Set	74
29	Effects of Beam Current on Impingement Current for the 15-cm SHAG Set	75
30	Effects of Beam Current on the Background- and Source-Dominated-Impingement Current Fractions for the 7-hole, 1/2-cm Grid Set	77
31	Effects of Beam Current on the Background- and Source-Dominated-Impingement Current Fractions for the 15-cm SHAG Set	78
A1	A Hypothetical Probe Surface Submerged in an Ambient Plasma	87
A2	A Hypothetical Probe Surface Submerged in an Ambient Plasma with an Ion Beamlet	89
A3	A Hypothetical Probe Surface Submerged in an Ion Beamlet	91
A4	Effects of the Reference Potential on the Hot-Filament, Emissive-Probe, Floating Potential	93

I. Introduction

Ion thrusters generate thrust by ionizing atoms (supplied as a neutral propellant gas) and then expelling them at high velocities in an ion beam. These ions are produced within a thruster (Fig. 1) that consists of 1) a discharge chamber, 2) a hollow cathode, 3) an anode, 4) a screen grid, 5) an accel grid, and 6) a neutralizer. A potential difference (the discharge voltage) is applied between the hollow cathode (an electron source) and the anode (an electron collection surface) to accelerate electrons (depicted as small solid circles) to modest kinetic energies. Ionization occurs when one of these modest-kinetic-energy electrons strikes an atom (open circles), losing some of its initial energy, and causing the ejection of an electron from the atom. Each electron-impact-ionization collision, therefore, produces one ion, a lower-energy-incident electron, and an ionization-ejected electron. Since the incident and ionization-ejected electrons frequently have insufficient kinetic energy to ionize additional atoms, they are removed from the discharge chamber as a current to the anode (the discharge current). The resulting collection of mobile ions and electrons within the discharge chamber is called the discharge plasma and it is from this plasma that ions are extracted to form the high velocity ion beam. The extraction of the ions is accomplished using the screen and accel grids (referred to together as the grid set) which are typically two convex plates having many aligned apertures. As Fig. 1

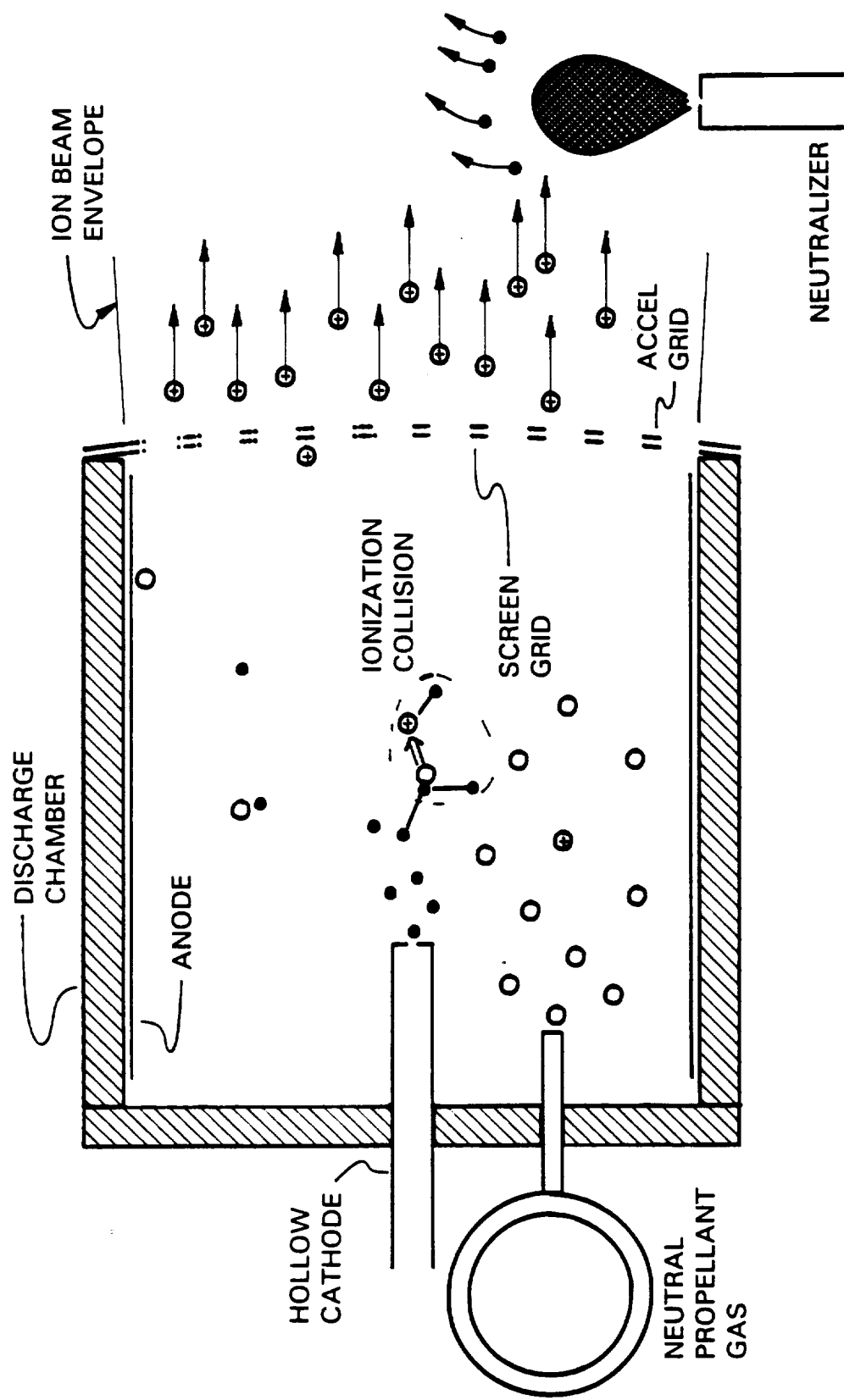


Fig. 1 Sketch of a Typical Ion Thruster

shows the screen grid is typically connected directly to the discharge chamber whereas the accel grid is electrically isolated from the screen grid and discharge chamber. This mechanical configuration allows a positive potential (the screen grid potential) on the order of a few thousand volts to be applied to the screen grid and discharge chamber while a negative potential (the accel grid potential) on the order of a few hundred volts is applied to the accel grid. This combination of potentials accelerates the ions from the discharge plasma and creates a beam of ions with velocity vectors (depicted by the arrows on Fig. 1) that are generally directed downstream, away from the thruster within a rather well-defined envelope. For ion thrusters that utilize grid sets that are designed and operated properly, these extracted ions leave the thruster without striking the accel grid. However, if the ion thruster is improperly operated or the grid set is poorly designed it is possible that a portion of the ions created within the discharge chamber will strike the accel grid. This phenomenon of direct ion impact on the accel grid is called direct impingement and for most of the thrusters and grid sets in use today it has been reduced to a negligible level by proper operation and design. Lastly, to satisfy conservation of charge and prevent the thruster from charging negatively, electrons must be injected into the ion beam at a rate equal to the ion extraction rate. This electron ejection is accomplished using the neutralizer (similar in design to the ion-thruster hollow cathode) to create a downstream ambient plasma from which an electron current is extracted as suggested by Fig. 1.

As a consequence of the method by which they develop thrust, ion thrusters operate at very small propellant flow rates and as a result the thrust level they achieve is small, typically tens to a few hundred milli-newtons [1,2]. This low propellant flow rate leads to small propellant mass requirements, and this along with the high propellant exhaust velocities (i.e., a high specific impulse) makes ion thrusters more attractive than conventional chemical and cold gas thrusters for many space missions. Specifically, these thrusters have been investigated for use on interstellar missions [3], interplanetary and comet/asteroid rendezvous missions [4,5], orbit raising missions [6], and north-south stationkeeping of communication satellites [7]. The low flow rates and thrust levels, however, also make the time required to complete some of these mission quite large, e.g., from one to five years [4]. Ion thrusters typically operate throughout most of a mission so demonstrations of long thruster lifetimes (tens of thousands of hours) are critically important to their acceptance and eventual use. Several experiments [8,9] were conducted in terrestrial facilities to measure ion-thruster lifetimes and they concluded that mercury-propellant ion thrusters could complete missions requiring operating times over 10,000 hours without any major failures. The propellant used for ion thrusters, however, was changed from mercury to xenon and this necessitated repeating the tests using xenon. The results of these new tests were quite surprising because failures were observed after only a few thousand hours of operation [10,11,12,13]. Post-test analysis revealed that xenon-propellant thrusters failed because as material was eroded from the accel grid, small-metallic flakes were formed. These flakes would eventually electrically short the two

grids together and prevent the application of the high voltages required to extract the ions. This erosion (termed sputter erosion) of accel grids is due to ions striking the grid with enough energy to cause the ejection of material which can then be deposited on other surfaces. Sputter erosion of accel grids has always been observed but the rates associated with xenon-propellant thrusters were approximately four times greater than that observed on mercury-propellant thrusters [11]. Since the rate at which atoms are sputtered away is proportional to the ion arrival rate, the sputter-erosion rate is proportional to the current of ions impinging on the accel grid (the impingement current). It has been shown that during typical xenon-propellant experiments this current is approximately four times that measured during experiments on mercury-propellant thrusters. It is believed that this quadrupling of the impingement current is responsible for the decrease in xenon-thruster lifetimes.

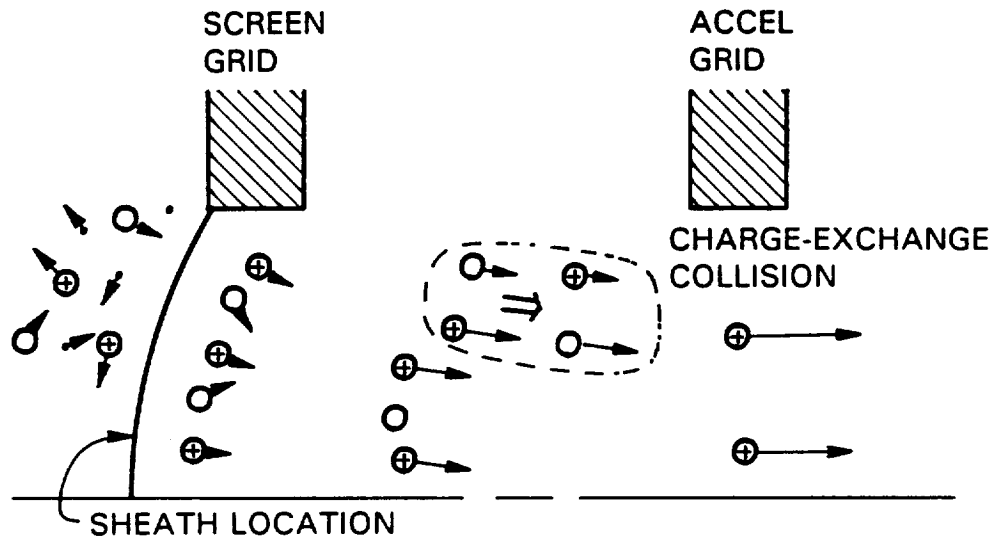
To find the origin of this four-fold increase in impingement currents associated with xenon-ion thrusters, a model developed and verified by Kerslake [14] to predict impingement currents for mercury-ion thrusters was applied to xenon thrusters. This model which will be discussed in the theoretical section yielded computed-xenon impingement currents that were an order-of-magnitude less than those actually measure during thruster operation [15]. The experimental investigation and model-revision work to be described in this dissertation was undertaken to 1) identify the deficiency (ies) in the Kerslake model leading to the order-of-magnitude difference between the computed- and measured-xenon impingement currents, 2) revise and enhance this model to correct for these identified deficiencies and 3) verify the

accuracy of this new model over a range of xenon-thruster operating conditions using several grid-set geometries.

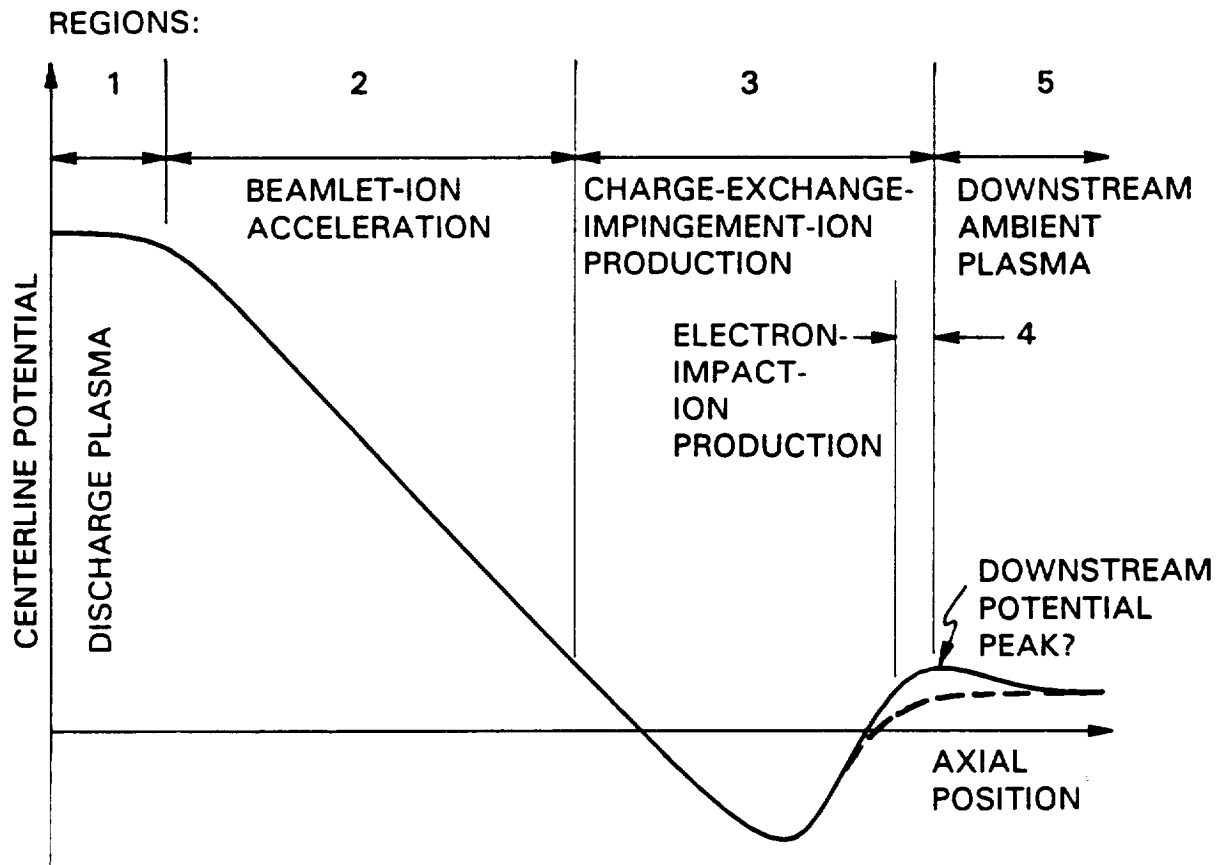
II. Theoretical Development of a One-Dimensional Impingement Current Model

A. Impingement Ion Production Mechanisms

To understand how impingement-current ions are created it is instructive to examine how ions are extracted from the discharge plasma forming the individual ion beamlets. A sketch of a screen/accel grid aperture pair is shown on the upper portion of Fig. 2 and it will be used to aid in the discussion. As previously stated, ions are extracted from the discharge plasma by applying positive and negative potentials to the screen and accel grids, respectively, and this creates a potential profile along the aperture centerline similar to that sketched on the bottom of Fig. 2. This lower sketch also identifies five separate regions within which different phases of ion acceleration occur. Upstream of the screen grid, within the discharge-plasma region (Region 1), there exist ions, electrons, and neutral atoms randomly moving at their respective thermal speeds. These particles can eventually migrate downstream toward the potential boundary between the constant potential of the discharge plasma and the steep potential gradient created by the screen and accel grid potentials. At this potential boundary (the sheath) ions begin their downstream acceleration process, electrons are reflected back into the discharge plasma, and the neutral propellant atoms (having no net charge) proceed downstream unaffected by the potential



a) Physical Diagram of Ion Beamlet Formation



b) Corresponding Centerline Potential Profile

Fig. 2 Ion Beamlet Definitions

gradients. As suggested in the upper sketch, ions move through the beamlet-ion acceleration region (Region 2) and gain kinetic energy (indicated by the longer arrows), while the neutrals flow through unaffected. These two groups of particles, typically, move through the beamlet-ion acceleration region without interacting, however, occasionally a charge-exchange collision can occur. As suggested in the upper sketch, a charge-exchange event involves the transfer of an electron from a neutral atom to a beamlet ion. This event results in a charge-exchange ion with the neutral atom's pre-event kinetic energy and an atom with the ion's pre-event kinetic energy. The beamlet and charge-exchange ions continue to accelerate as they move through the charge-exchange impingement-ion production region (Region 3). On the other hand, the kinetic energies of the neutral atoms from the discharge chamber and those resulting from charge-exchange collisions remain constant throughout the region. Both the beamlet and charge-exchange ions reach their maximum kinetic energies at the potential minimum near the accel grid before they decelerate somewhat as they exit the region. Neutral atoms and beamlet ions are also present in Region 3, hence charge-exchange collisions can occur there as well. The difference between charge-exchange ions created there and those created in Region 2 is that those from Region 3 are unable to gain the kinetic energy required to escape the potential well created by the accel grid. Therefore, all charge-exchange ions created within Region 3 will impinge on, and sputter erode the accel grid. In contrast, the beamlet ions and those charge-exchange ions created within Region 2 generally escape the accel-grid potential well and enter the downstream-ambient-plasma region (Region 5)

with kinetic energies determined by either the screen-grid potential or the potential at which the charge-exchange ions were created. As described earlier, the neutralizer prevents negative charging of the thruster by creating an ambient plasma from which electrons are injected into the ion beam at a rate required to satisfy conservation of charge. Both beamlet ions and neutral atoms are present within Region 5, hence it is possible for charge-exchange ions to be created within this region also. Whether or not these ions will impinge on the accel will depend on the potential environment downstream of the accel grid. For example, if the potential structure is similar to that shown by the solid line exists, i.e., a downstream-potential peak exists, all the charge-exchange ions created in Region 5 will find themselves in a potential gradient that directs them away from the accel grid. However, if the potential structure is more like that shown by the dashed line (no potential peak) then there is a finite probability that charge-exchange ions created in Region 5 will impinge on the accel grid. Since the potential structure of the downstream-ambient plasma is uncertain, part of this work will involve making potential measurements in this region. Until these data are presented, cases reflecting both the existence and lack of the downstream-potential peak will be considered.

If the potential peak does exist, it could not only prevent Region-5-charge-exchange ions from impinging on the accel grid, but it could accelerate electrons available in the downstream-ambient plasma to modest kinetic energies near the peak shown in Fig 2. These electrons could then have electron-impact-ionization collisions with neutral atoms and create additional ions that could impinge on the accel grid. If

such collisions were to occur within Region 5, the resulting (electron-impact) ions would behave like charge-exchange ions and the potential gradients would accelerate them away from the accel grid. If, however, the ions were created upstream of the downstream-potential peak (within Region 4) the potential gradients would accelerate them into the accel grid and they would contribute to the impingement current. However, if the downstream-potential peak does not exist then ambient-plasma electrons will not be accelerated to modest energies, electron-impact-ionization collisions will not occur, Region 4 would not exist, and consequently electron-impact ionization would not contribute to the production of impingement-current ions. In addition, the lack of this potential peak will allow some charge-exchange ions created within Region 5 to impinge on the accel grid.

To calculate the probability that a Region-5-charge-exchange ion will impinge on the accel grid, in the absence of the potential peak, it is assumed 1) there are no potential gradients in the ambient plasma, 2) the velocity distribution of the neutral atoms can be described using an isotropic distribution, and 3) the probability that a charge-exchange ion will impinge is only dependent on the axial position at which the ion was created (a one-dimensional approximation). The probability that a Region-5-charge-exchange ion will impinge under these circumstances can be understood using Fig. 3. This figure shows the solid angle (Ω) from an axial position, z , (where the ion was created) subtended by the exposed accel grid. Using the aforementioned assumptions the probability that an ion will strike the grid is equal to the ratio of Ω to the total solid angle through which the ion can leave (4π). This ratio of solid angles,

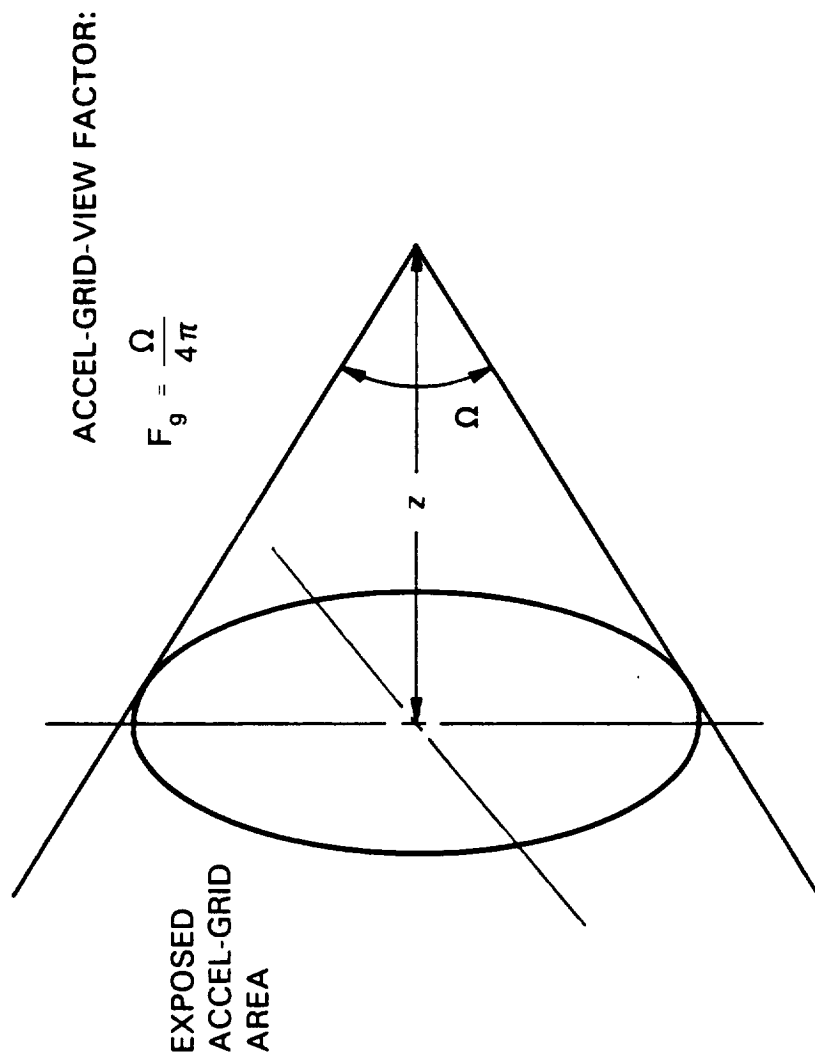


Fig. 3 Accel-Grid-View Factor Definition

the accel-grid-view factor $[F_g]$, is given by

$$F_g = \frac{1}{2} \left\{ 1 - \frac{z}{[r_a^2 + z^2]^{1/2}} \right\} , \quad (1)$$

where r_a is the exposed-accel-grid radius which is determined by grid geometry and need not necessarily be equal to the active radius of the accel grid (i.e., the radius through which the ion beam is extracted).

B. One-Dimensional Impingement-Ion-Production Model

The previous discussion has suggested that impingement-current ions are produced via charge-exchange collisions within Region 3 and possibly by either electron impact-ionization collisions within Region 4 or charge-exchange ions created within Region 5. Therefore, in its most general form (i.e., neglecting the probability that these ions will impinge on the grid), the equation used to calculate the impingement current would sum the rates at which charge-exchange and electron-impact ions are created in each region. The frequency at which beamlet ions have charge-exchange collisions with neutral atoms is given by [16]

$$\nu = n_o \sigma_{ce} v_B , \quad (2)$$

where n_o is the density of neutral atoms (i.e., the particles being struck), σ_{ce} is the charge-exchange cross-section, and v_B is the relative beamlet-ion/neutral-atom speed which in this case is just the beamlet-ion speed. The rate at which charge-exchange

ions are created within a differential volume ($d\dot{n}_{ce}/dV$), having a beamlet-ion density of n_B , is equal to the ion-density/collision-frequency product and is given by

$$\frac{d\dot{n}_{ce}}{dV} = n_B n_o \sigma_{ce} v_B \quad . \quad (3)$$

Similarly, the rate at which impingement-current ions are created via electron-impact ionization within a differential volume ($d\dot{n}_{ei}/dV$) is given by

$$\frac{d\dot{n}_{ei}}{dV} = n_e n_o \sigma_e v_e \quad , \quad (4)$$

where n_e is the electron density, σ_e is the impact-ionization cross-section, and v_e is the mean difference between the electron and atom speeds, essentially the electron speed.

The total production rate for impingement-current ions ($d\dot{n}_i$) by both charge-exchange and electron-impact ionization collisions is, therefore, given by

$$d\dot{n}_i = \frac{d\dot{n}_{ce}}{dV} dV + \frac{d\dot{n}_{ei}}{dV} dV = n_B n_o \sigma_{ce} v_B dV + n_e n_o \sigma_e v_e dV \quad . \quad (5)$$

To simplify the evaluation of Eq. 5, a one-dimensional approximation is imposed and the equation becomes

$$\begin{aligned} d\dot{n}_i(z) &= n_B(z) n_o(z) \sigma_{ce}(z) v_B(z) A_B(z) dz \\ &+ n_e(z) n_o(z) \sigma_e(z) v_e(z) A_e(z) dz \quad , \end{aligned} \quad (6)$$

where $A_B(z)$ is the ion beamlet cross-sectional area and $A_e(z)$ is the cross-sectional area of the region of electron-impact ionization associated with each beamlet. If all impingement-current ions are assumed to be created with a single electronic charge,

Eq. 6 can be multiplied by this charge (e) to obtain the differential impingement-current created within the length dz

$$d\hat{J}_i(z) = \hat{J}_B n_o(z) \sigma_{ce} dz + e n_e(z) n_o(z) \sigma_e(z) v_e(z) A_e(z) dz, \quad (7)$$

where the charge-exchange cross-section, which is a weak function of the beamlet ion speed, has been assumed to be constant with axial position and the following expression for the beamlet-ion current (\hat{J}_B) has been used.

$$\hat{J}_B = e n_B(z) v_B(z) A_B(z). \quad (8)$$

The total accel-grid impingement current can be calculated by integrating Eq. 7 over the regions in which the charge-exchange and electron-impact-ionization ions that impinge on the accel grid are created. As mentioned previously, all charge-exchange ions produced within Region 3 impinge on the accel grid whether or not there is a downstream-potential peak. On the other hand, the existence of the downstream-potential peak does determine whether or not electron-impact ions from Region 4 or portions of the charge-exchange ions produced in Region 5 will impinge on the accel grid. If the peak exists, the impingement current per ion beamlet is calculated by integrating

$$\begin{aligned} \hat{J}_i = & \hat{J}_B \sigma_{ce} \int_{\ell_3} n_o(z) dz \\ & + e \int_{\ell_4} n_e(z) n_o(z) \sigma_e(z) v_e(z) A_e(z) dz \quad , \end{aligned} \quad (9)$$

where ℓ_3 and ℓ_4 are the lengths of regions 3 and 4, respectively. However, if the downstream-potential peak does not exist then the total impingement current per ion beamlet is given by

$$\begin{aligned} \hat{J}_i = & \hat{J}_B \sigma_{ce} \int_{\ell_3} n_o(z) dz \\ & + \hat{J}_B \sigma_{ce} \int_{\ell_5} F_g n_o(z) dz \quad , \end{aligned} \quad (10)$$

where the second integral represents the fraction of charge-exchange ions created in Region 5 that will impinge on the accel grid. Of the parameters appearing in the charge-exchange terms of Eqs. 9 and 10, the beamlet-ion current is easily measured and the charge-exchange cross-section is available in the literature [17,18,19]. Hence these terms could be evaluated if the neutral-density profile and the length of Region 3 were known. In contrast, most of the terms in the electron-impact component of Eq. 9 are difficult to measure experimentally or compute theoretically. Hence it is desirable to determine if the electron-impact term is significant relative to the charge-exchange terms before much effort is spent trying to develop the equations further.

C. An Order-of-Magnitude Comparison between the Impingement Current
Fractions Created by Charge-Exchange and Electron-Impact Ionization

To find out if the rate of electron-impact ionization in Region 4 is small compared to the rate of charge-exchange ion production in Region 3, a simple order-of-magnitude comparison was performed. For this comparison, the magnitude of the charge-exchange term is estimated from the first term of Eq. 9 by assuming the neutral density downstream of the accel grid is constant. Substituting this constant density into the equation and integrating yields

$$\dot{J}_{i_{ce}} = \dot{J}_B \sigma_{ce} n_o \ell_3 \quad . \quad (11)$$

To estimate the electron-impact term of Eq. 9, it was assumed that 1) the electron and ion densities were equal ($n_e \approx n_B$), 2) the areas A_e and A_B were equal, and 3) that the neutral density and ionization cross-section were independent of axial position. In this case, the second term of Eq. 9 simplifies and can be integrated to obtain

$$\dot{J}_{i_e} = \dot{J}_B n_o \sigma_e \ell_4 \sqrt{\frac{v_e}{v_B}} \quad . \quad (12)$$

The ratio of Eqs. 11 and 12 is the ratio of the current created by charge-exchange collisions to that created by electron-impact-ionization collisions, i.e.,

$$\frac{\dot{J}_{i_{ce}}}{\dot{J}_{i_e}} = \frac{\sigma_{ce} \ell_3}{\sigma_e \ell_4} \sqrt{\frac{v_B}{v_e}} \quad . \quad (13)$$

Using a charge-exchange cross-section of $50 \times 10^{-16} \text{ cm}^2$ [18], the maximum impact-ionization cross-section of $1 \times 10^{-16} \text{ cm}^2$ [20], ion and electron speeds of 38,000 m/s ($\sim 1000 \text{ eV}$) and 470,000 m/s ($\sim 0.5 \text{ eV}$), respectively, and assuming ℓ_3 and ℓ_4 are equal (an over estimation for ℓ_4), Eq. 13 gives a value of 14. This result shows that charge-exchange ion production should dominate even when assumptions favoring electron-impact ionization are used.

It has also been suggested that multi-step electron-ionization may contribute ions to the impingement current. Multi-step electron-ionization involves electrons with energies less than the atomic ionization-potential that strike atoms and creating metastable neutrals. These metastable neutrals may be ionized by a second collision with an electron. A conservative over estimate of the multi-step production rate can be obtained by assuming that the metastable density in the discharge chamber persists throughout Region 4 (i.e., that the metastable lifetime is long). Substituting the metastable atom density (\tilde{n}_o), Eq. 12 yields the impingement-ion current per beamlet due to electron impact ionization of metastables (\tilde{J}_{i_e}) namely

$$\tilde{J}_{i_e} = J_B \tilde{n}_o \sigma_e \ell_4 \sqrt{\frac{v_e}{v_B}} \quad . \quad (14)$$

The ratio of impingement current created by charge-exchange to that produced by multi-step electron-impact ionization is, therefore, given by

$$\frac{\hat{J}_{i_{\infty}}}{\hat{J}_{i_e}} = \frac{\sigma_{ce} n_o}{\sigma_e \bar{n}_o} \sqrt{\frac{v_B}{v_e}} \quad (15)$$

Again using typical numbers for the collision cross-sections, particle velocities, and noting that the metastable density where they are produced (in the discharge chamber) is at least an order-of-magnitude smaller than the ground-state neutral density, this equation suggests that the current due to charge-exchange collisions is at least 140 times that due to multi-step ionization.

Based on these two, order-of-magnitude calculations it has been concluded that both single- and multi-step-electron-impact-ionization collisions are negligible compared to charge-exchange collisions. This suggests that the total impingement current per ion beamlet can be calculated by 1) integrating the charge-exchange term of Eq. 9 if the downstream-potential peak exists or 2) integrating both terms of Eq. 10 if it does not.

D. An Approximation of the Neutral Density Profile

The remaining obstacles to determining the total impingement current per ion beamlet are the neutral density profile ($n_o(z)$) and the length of Region 3 (ℓ_3). The neutral density profile can be calculated by assuming it is composed of two components: first, the source-dominated-density profile which is determined by the propellant flow through the grid set, and second, the constant background density component due to residual atoms present within any vacuum system having a finite

pumping speed. The source-dominated profile can be estimated using a Monte-Carlo simulation procedure developed for radiative-heat-transfer calculations [21]. This procedure was chosen because ion thrusters typically operated at low pressures where collisions between neutral propellant atoms are infrequent, hence, free-molecular flow can be used to describe the passage of atoms through the grid set. In this flow regime the motion of the particles through the grid set is similar to that of photons moving through an axi-symmetric radiative enclosure.

The axi-symmetric radiative geometry used to model the neutral atom flow through a single aperture pair within a grid set is pictured on Fig. 4. Grid surfaces and other domain boundaries are presented on the figure as being either perfectly diffuse (complete absorption and outward re-emission with a cosine of the emission angle distribution), perfectly specular (angle-of-incidence equals angle-of-reflection), or black (complete absorption and no re-emission). As an initial approximation, this model assumes that the surface located downstream of the accel grid and between this and the adjacent aperture is black, i.e., the neutral density contribution from adjacent apertures is not included in these calculations. To model multi-aperture grid-sets accurately, this downstream surface would need to be grey-specular with a grey scale becoming increasingly black with downstream (axial) distance and for holes near the periphery of the grid set.

The simulation procedure applied to the geometric and boundary conditions of Fig. 4 involves tracking neutral particles (which behave like photons) as they are emitted from the planar, discharge-plasma-emission surface, move throughout the

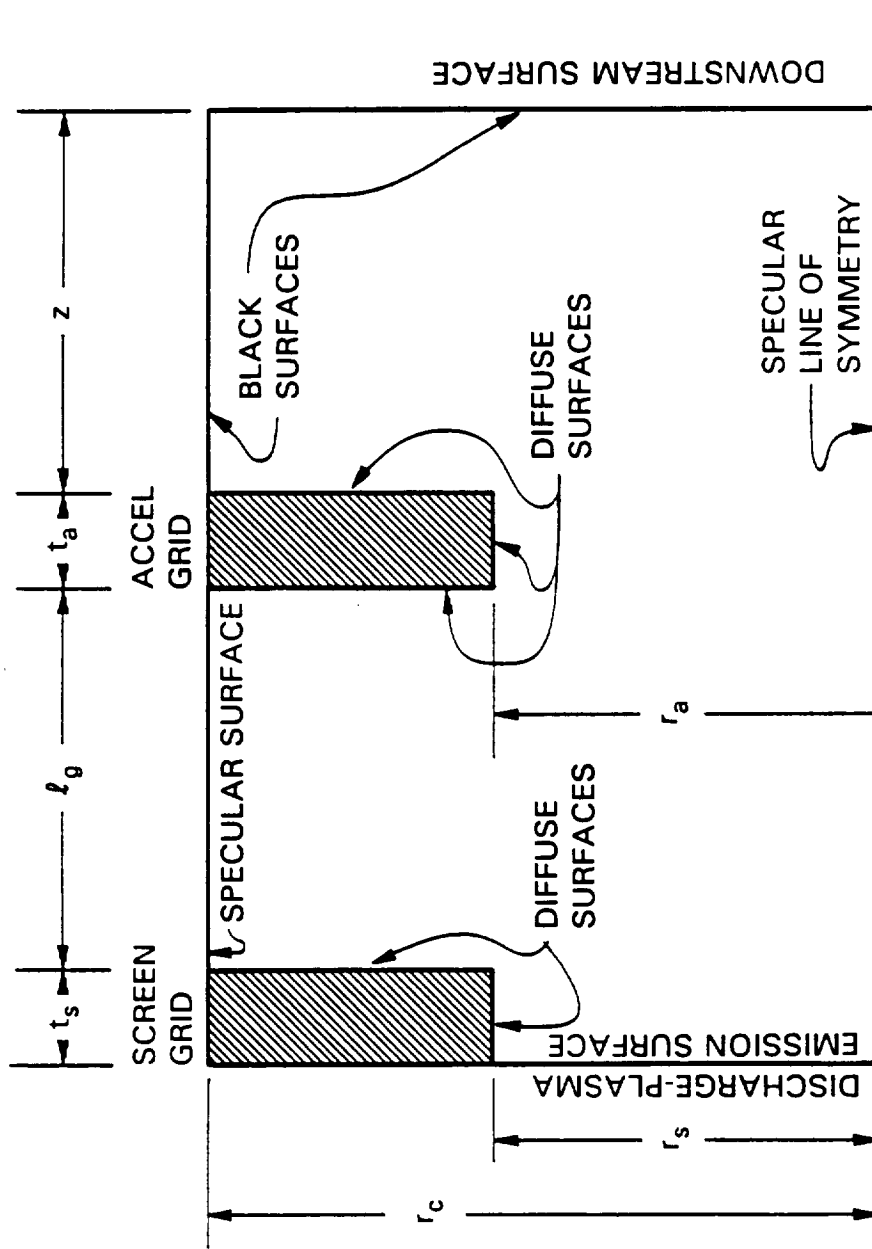


Fig. 4 Monte-Carlo Simulation Geometry

domain and are then absorbed on one of the two black surfaces. The neutral particles are emitted from the emission surface with an equal probability in all downstream directions as opposed to normal emission. This diffuse emission is believed to be a more accurate representation of the neutral flow from the discharge chamber. The neutral-density profile at the downstream surface (an axial position z) is determined by 1) counting as a function of radius the number of emitted particles absorbed (the number of neutrals that would cross this surface per unit simulation time), 2) converting this radial-count-profile to flux v. radial position (i.e., neutrals/cm²/sec) through division by the area of the downstream-surface segments and 3) dividing by the mean speed of propellant atoms at the discharge-chamber temperature to obtain a radial, propellant-density profile associated with flow from the source. This radial density profile is then normalized through division by the total number of atoms emitted from the discharge-chamber-emission surface to obtain the source-neutral-density profile. The simulation procedure is repeated for several z values to obtain the complete, axisymmetric, normalized-source-density field from which the normalized-centerline-source-density profile is obtained. The circular-data points presented on Fig. 5 show results obtained using the typical grid-set geometry defined in the legend. To approximate these Monte-Carlo results, the exponential curve fit (shown as the solid line) and given by

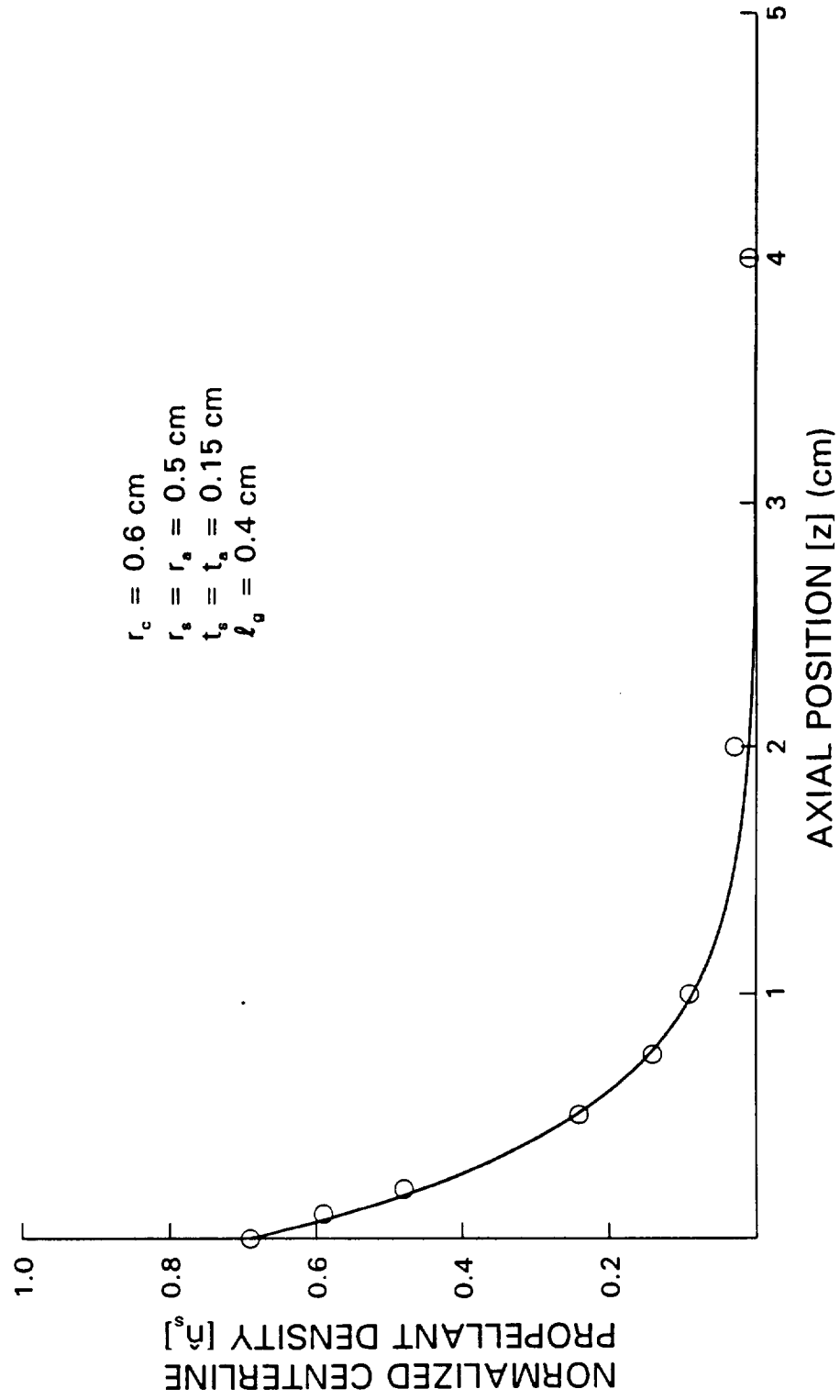


Fig. 5 Monte-Carlo Simulation Results and the Corresponding Exponential Curve Fit

$$\hat{n}_s = F_s \exp \left[\frac{-z}{\ell_s} \right] \quad (16)$$

is used. In this equation \hat{n}_s is the normalized-centerline-propellant density, F_s is the source-neutral exit fraction and ℓ_s is the source-neutral-expansion length. The curve fit of Fig. 5 was obtained using an expansion length ℓ_s of 0.48 cm and an exit fraction F_s of 0.69. The source-neutral exit fraction of 0.69 implies that for this grid set geometry 69% of the neutrals emitted from the discharge-emission surface actually exit through the accel grid aperture while 31% are reflected off surfaces within the grid set and go back into the discharge chamber.

The exponential curve fit of Eq. 16 is an estimate for the normalized-centerline-source-density profile that can be multiplied by the neutral density within the discharge chamber (n_s) to obtain the source-dominated-density profile. However, the actual atom-density profile downstream of the accel grid is a combination of this source-dominated-density profile and the constant background density. The actual atom density (n_o) is therefore given by

$$n_o = n_s F_s \exp \left[\frac{-z}{\ell_s} \right] + n_b \quad , \quad (17)$$

where n_b is the background atom density that is calculated knowing the vacuum chamber pressure.

E. Evaluation of the Differential-Impingement-Current Integral

Using the approximation for the neutral density profile and assuming no downstream-potential peak (Fig. 2) is present, the impingement current is calculated by substituting Eq. 17 into Eq. 10. If experimental data show that the downstream-potential peak exists, then some terms in the resulting equation will be deleted to obtain the impingement current due to charge-exchange collisions within Region 3 only. Substituting the neutral density profile into Eq. 10 yields the following equation for the impingement current per ion beamlet

$$\begin{aligned} \hat{J}_i = & \hat{J}_B \sigma_{ce} \int_0^{\ell_3} \left\{ n_s (1 - \eta_u) F_s \exp \left[\frac{-z}{\ell_s} \right] + n_b \right\} dz \\ & + \hat{J}_B \sigma_{ce} \int_{\ell_3}^{\infty} F_g \left\{ n_s (1 - \eta_u) F_s \exp \left[\frac{-z}{\ell_s} \right] + n_b \right\} dz, \end{aligned} \quad (18)$$

where η_u is the propellant utilization, defined as the ratio of the beamlet current extracted from the thruster to the neutral propellant supplied (expressed as a current). The term $(1 - \eta_u)$, therefore, accounts for the reduction in the source-dominated density at a fixed input flow as the beamlet current increases. In evaluating this integral, the upstream boundary of Region 3 is chosen as the origin and Region 5 has been assumed to be bounded on the upstream side by Region 3 and unbounded on the downstream side. The expression for the source-dominated-impingement current ($\hat{J}_{i,s}$) component of the total impingement current per ion beamlet is given by

$$\begin{aligned} \dot{J}_{i,s} = & \dot{J}_B \sigma_{ce} n_s (1 - \eta_u) \ell_s F_s \left\{ 1 - \exp \left[\frac{-\ell_3}{\ell_s} \right] \right\} \\ & + \frac{\dot{J}_B \sigma_{ce} n_s (1 - \eta_u) F_s}{2} \left\{ \ell_s \exp \frac{-\ell_3}{\ell_s} - \int_{\ell_3}^{\infty} \frac{\exp [-z / \ell_s] z}{[r_a^2 + z^2]^{1/2}} dz \right\}, \end{aligned} \quad (19)$$

where the last integral must be evaluated numerically. Completing the evaluation of Eq. 18 yields the following equation for the background-dominated-impingement current ($\dot{J}_{i,b}$)

$$\dot{J}_{i,b} = \frac{\dot{J}_B \sigma_{ce} n_b}{2} \left[(r_a^2 + \ell_3^2)^{1/2} + \ell_3 \right]. \quad (20)$$

The total impingement current per ion beamlet is obtained by summing the source- and background-dominated impingement currents, i.e.,

$$\dot{J}_i = \dot{J}_{i,s} + \dot{J}_{i,b}. \quad (21)$$

It should be noted that all the equations presented to this point yield impingement currents per ion beamlet (\dot{J}_i). The total impingement current (\dot{J}_i) (which can be then directly compared to experimentally measured values) is obtained by summing the results of Eq. 21 for all the apertures in a grid set. This summation can be completed by realizing that the summation of the individual beamlet ion currents is the total beam current (\dot{J}_B). Therefore, the total impingement current can be calculated by substituting the total beam (\dot{J}_B) into Eqs. 19 and 20 for the beamlet current (\dot{J}_B) to yield

$$\begin{aligned}
J_i = & J_B \sigma_{ce} n_s (1 - \eta_u) \ell_s F_s \left\{ 1 - \exp \left[\frac{-\ell_3}{\ell_s} \right] \right\} \\
& + \frac{J_B \sigma_{ce} n_s (1 - \eta_u) F_s}{2} \left\{ \ell_s \exp \frac{-\ell_3}{\ell_s} - \int_{\ell_3}^{\infty} \frac{\exp [-z / \ell_s] z}{[r_a^2 + z^2]^{1/2}} dz \right\} \\
& + \frac{J_B \sigma_{ce} n_b}{2} \left[(r_a^2 + \ell_3^2)^{1/2} + \ell_3 \right] .
\end{aligned} \tag{22}$$

However, if one only needs an estimate of the impingement current, the source-neutral expansion length can be assumed to be equal to the length of Region 3 (i.e., $\ell_s \approx \ell_3$), the integral of Eq. 22 can be neglected, and the length of Region 3 can be assumed small compared to the exposed-accel grid area. Using these assumptions yields the following approximation for the total impingement current

$$\begin{aligned}
J_i \approx & J_B \sigma_{ce} \left[\frac{2}{3} F_s (1 - \eta_u) n_s \ell_3 \right] \\
& + J_B \sigma_{ce} n_o \frac{d_a}{4} .
\end{aligned} \tag{23}$$

In this equation the first term is the approximation for the source-dominated component and the second is the approximation for the background-dominated component. Equation 23 shows that the characteristic length for charge-exchange production within Region 3 (source-dominated) is ℓ_3 whereas the characteristic length for charge-exchange ion production in the downstream-ambient plasma (background-dominated) is $1/4$ of the exposed accel grid diameter (d_a).

F. Simplification of the Comparison Between Theoretical and Experimental Measurements for the Length of Region Three

Kaufman [22] developed a one-dimensional model to determine the potential structure between two hypothetical surfaces at known potentials and between which ions are flowing at a prescribed current density. Using this model an equation for the distance between the two surfaces required to assure a zero-electric field at the second surface was determined. Kerslake [14] observed that there should be a zero electric field at the boundary between Regions 3 and 5 and that this ambient-plasma boundary could be represented as the second hypothetical surface. Incorporating this into the model, he obtained the following approximation for the length of Region 3

$$\ell_3 = \left[\frac{A_B \beta V_T^{\frac{3}{2}} (R^{-\frac{3}{2}} + 3R^{-1} - 4)}{J_B} \right]^{\frac{1}{2}}, \quad (24)$$

where V_T is the total voltage (i.e., $V_+ + |V_-|$), R is the net-to-total voltage ratio (V_+ / V_T), and

$$\beta \equiv \frac{4\epsilon_0}{9} \sqrt{\frac{2e}{m_i}}. \quad (25)$$

In this definition of β , ϵ_0 is the permittivity of free space, e is the charge of the ion and m_i is the ion mass. To simplify the comparison between experimental and Kerslake values for ℓ_3 over a wide range of beamlet current, Eq. 24 will be cast in terms of normalized perveance-per-hole (P) [23]. Normalized perveance-per-hole is

the ratio of the actual beamlet current extracted from an aperture to the maximum current (for an ion charge-to-mass ratio of e/m_i) that can be extracted between two plates for an imposed potential-difference of V_T and separation-distance ℓ_e .

Specifically, normalized perveance-per-hole is given by

$$P = \frac{\dot{J}_B}{V_T^{3/2}} \left[\frac{\ell_e}{d_s} \right]^2 \left[\frac{\pi\beta}{4} \right]^{-1} \quad (26)$$

This equation is applied to ion thrusters, which extract current through axisymmetric apertures, by using a value for ℓ_e (the 1-D-effective-acceleration length) [24] approximated by

$$\ell_e = \left[\frac{d_s^2}{4} + (\ell_g + t_s)^2 \right]^{1/2}, \quad (27)$$

where ℓ_g is the screen-to-accel grid gap, d_s is the screen-grid aperture diameter, and t_s is the screen-grid thickness. Combining Eqs. 24 through 27 one obtains

$$\tilde{\ell}_n \equiv \frac{\ell_3}{\ell_e} = \left[\frac{(1 + 3R^{1/2} - 4R^{1.5})}{P} \right]^{1/2} \quad (28)$$

This defines the non-dimensional-neutralization length $[\tilde{\ell}_n]$ which will be used to compare experimentally measured values of ℓ_3 over a variety of beam currents and grid geometries.

III. Experimental Apparatus and Procedure

To obtain the data required to verify the preceding 1-D model for the impingement current, experiments were conducted using a Space Electric Rocket Test II (SERT II) ion thruster [25] that has been modified to accept various grid sets and utilizes independent inert gas flows through the main and cathode flow systems. The operation and control of the thruster was accomplished using the power supplies, voltmeters, and ammeters presented on Fig. 6. This figure shows the thruster, neutralizer, and power supplies required to establish and maintain the hollow cathode and thruster discharges, the neutralizer discharge, and to extract the ion beam. Specifically, the heater supply raises/sustains the cathode temperature, and the keeper and discharge supplies sustain electrical discharges between the cathode and keeper and the cathode and anode, respectively. It is these discharges that create the ions extracted from the discharge chamber that form the ion beam. The screen and accel grid power supplies apply the potentials required to extract this beam. The rate of ion extraction is measured using the beam current (J_b) ammeter and the rate of ion impact on the accel grid is measured by the impingement-current (J_i) ammeter. Also shown are the power supplies, volt meters and ammeters required to operate the neutralizer. The neutralizer uses heater and keeper supplies similar to those for the discharge chamber to heat this cathode and sustain its electrical discharge. The clamping diode

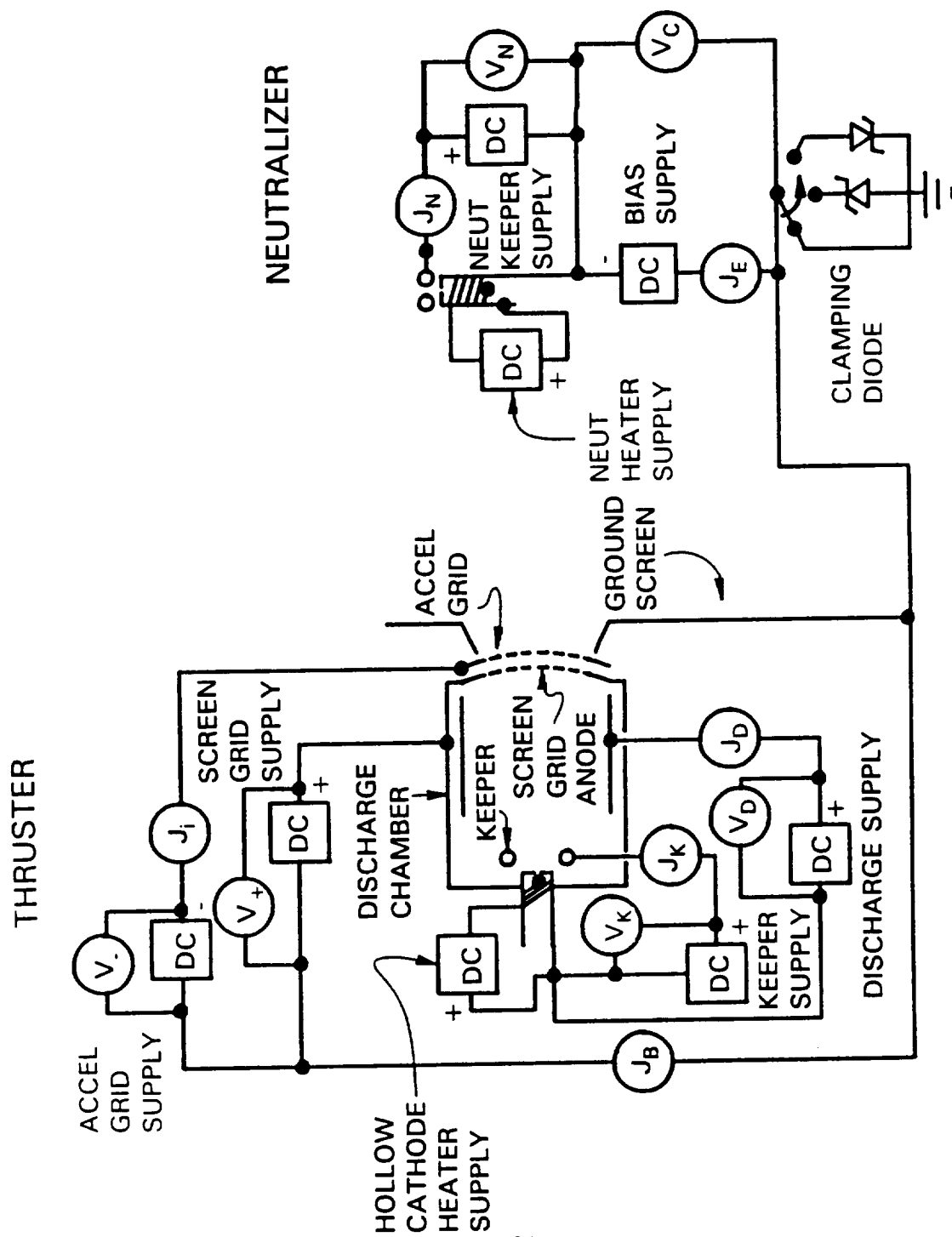


Fig. 6 Electrical Schematic

and bias supply control the electron emission (J_E) from the neutralizer and unless noted otherwise, the clamping diode was used to guarantee that the neutralizer emission current exactly matched the beam current.

A mechanical sketch showing the SERT II ion thruster, neutralizer, and the diagnostic-probe-positioning rod is given as Fig. 7. The figure shows how the hollow-cathode neutralizer was modified from the original SERT II design so it could be moved both axially and radially and so the neutralizer support tube would not be in the ion beam when the neutralizer is positioned at the beam edge. The neutralizer could be moved axially from 2 to 20 cm downstream of the accel grid and radially from the thruster centerline (0) to 30 cm from the centerline. The diagnostic-probe-positioning rod positioned different probes that each measured different properties of the ion beam and ambient plasma in the regions next to and immediately downstream of the accel grid. Either of the probes shown on Fig. 8 could be attached to the positioning rod to make the desired measurements.

The potential of the regions next to and immediately downstream of the accel grid was measured using the bent, hot-filament, emissive probe shown on Fig. 8a. In addition to the potential, the electron density and temperature of the ambient plasma were measured using the spherical Langmuir probe of Fig. 8b. As shown, the emissive probe is constructed from a 0.32-cm-dia, 2-hole-alumina tubing through which two stainless-steel, filament-support wires are passed. These wires support a 0.05 mm tungsten filament spot welded to form a 3-mm-by-3-mm loop. Williams [26] describes the circuitry used to heat the filament resistively to

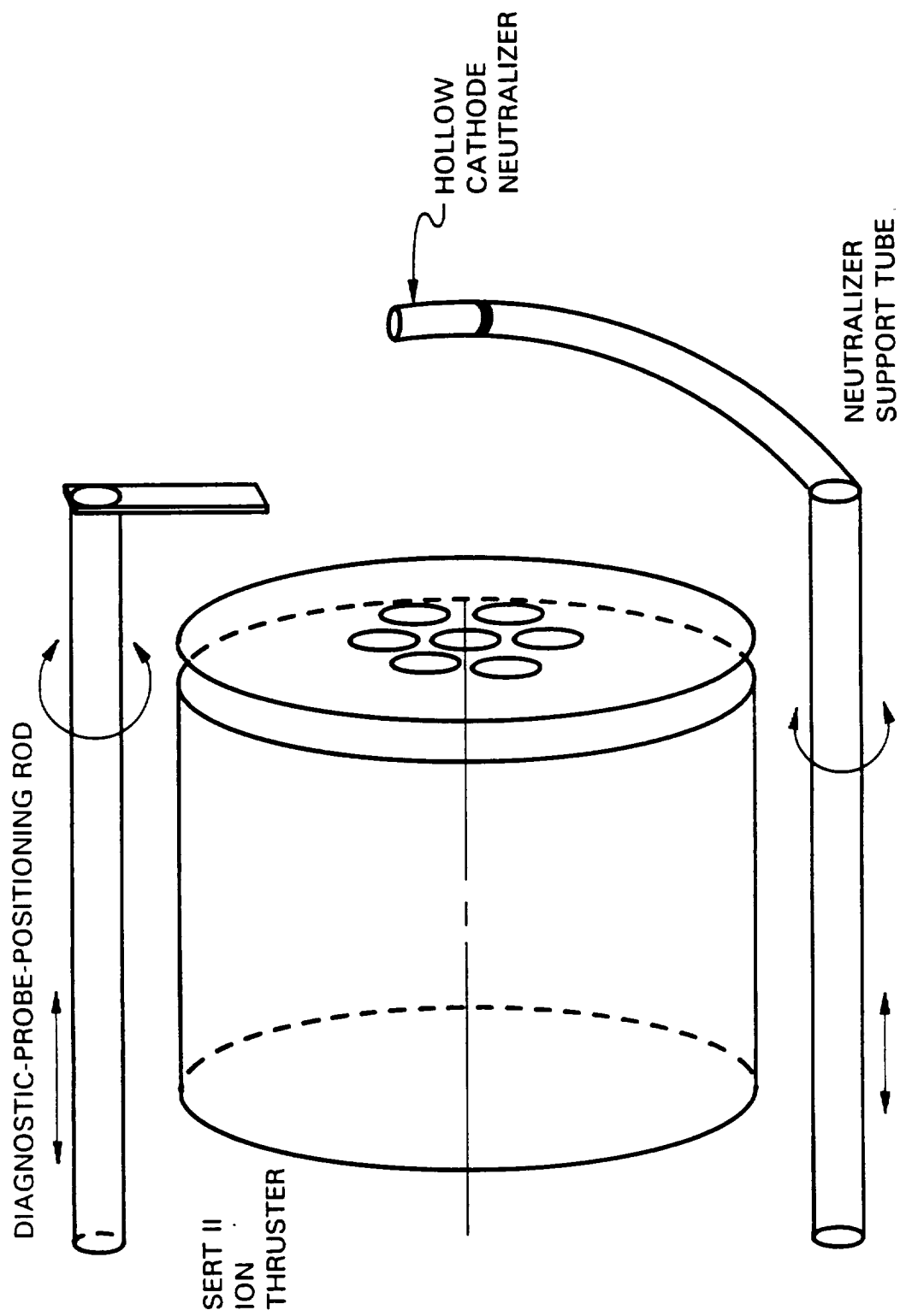


Fig. 7 Mechanical Schematic of the Experimental Apparatus

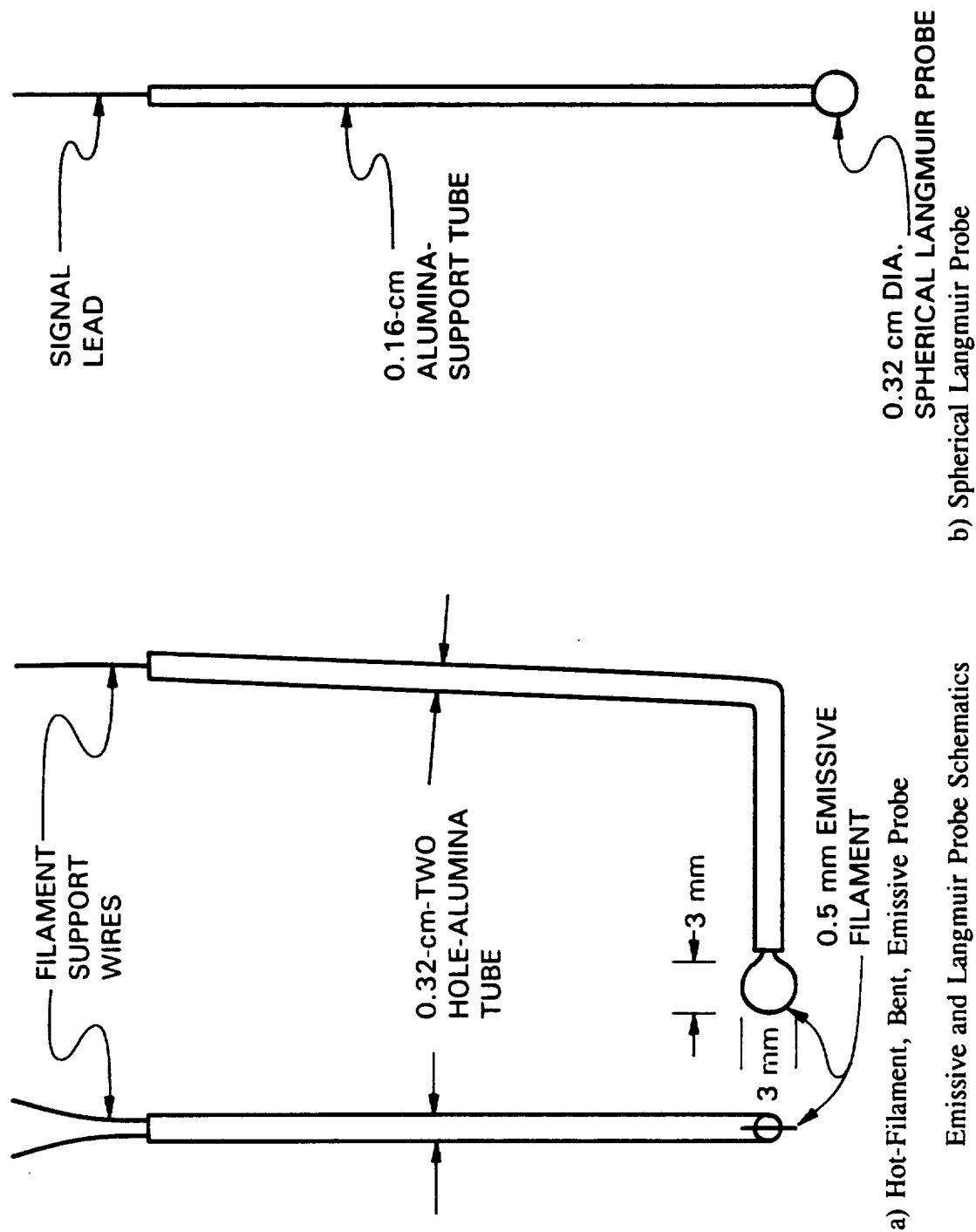


Fig. 8 Emissive and Langmuir Probe Schematics

incandescent (thermionic-emission) temperatures where in typical laboratory plasmas this probe will indicate potentials within a few volts of the local plasma potential [27]. In regions adjacent to the accel grid, however, high-energy ions and a depleted electron density (induced by the negative accel-grid potential) cause the emissive probe to float at potentials that can be significantly greater than the true potential. Fortunately, Smith, Hershkowitz and Coakley [28] have developed a method, referred to as the inflection point technique (IPT), that can be used to measure the potential in regions of low and unequal space-charge density like those near accel grids. The IPT method, as used in this study, involves measurement of the current collected or emitted by the probe as its potential is varied over a range from below to above the potential of the local environment (the local potential). For probe potentials greater than the local potential the probe collects electrons (if present) and for probe potentials less than the local potential it emits thermionically. Because the probe can emit electrons readily, the curvature of the probe-current-v.-voltage trace changes at the local potential making this point identifiable.

The Langmuir probe of Fig. 8b is constructed by passing a stainless steel lead through a 0.16 cm alumina tube and welding a 0.32 cm spherical stainless steel ball to the end of it. Electron density and temperature data are obtained by measuring the current collected by the probe as its potential is varied from tens of volts below to a few volts above plasma potential and analyzing these current-v.-voltage data using standard procedures [26].

The effects of grid-set geometries on the impingement currents and the

potential structure near the accel grid were determined using four different grid sets that could each be installed on the SERT II ion thruster. The first set is a conventional-high-perveance-15-cm SHAG (small-hole accel-grid) set similar to those developed for space applications. The second set (19-hole) has 19 apertures each having dimensions similar to those of the SHAG set but with a smaller overall beam diameter (1.2 cm). The final two grid sets were two 7-hole, large aperture sets used to make detailed potential measurements near the apertures and examine the effects of changes in the aperture diameter. Overall grid dimensions and characteristics for the normalized-centerline-propellant-densities profiles (obtained from the Monte-Carlo simulations) are summarized on Table 1. It should be noted that the SERT II grid region was masked down to accommodate both the 19-hole and both 7-hole grid sets on the thruster centerline. This assured uniform discharge-plasma properties across the upstream screen-grid surfaces of these grid sets.

All experiments were conducted in a 1.2-m-dia.-by-5.4-m-long, stainless-steel, diffusion-pumped vacuum tank. During each test the pressure was measured using a Schultz-Phelps-type, hot-filament ionization gauge [29] located approximately one meter downstream of the thruster. The gauge was calibrated for the two inert gasses used in this study by using a McLeod gauge capable of measuring pressures in the low 10^{-7} Torr range. The baseline (no flow) pressure in the vacuum tank was typically in the low 10^{-6} Torr range, and pressures measured during thruster operation were in the high 10^{-6} to low 10^{-5} Torr range.

Table 1
Summary of Grid-Set Parameters

Grid Designation	15-cm SHAG	19 hole	7-hole, 1-cm	7-hole, ½-cm
Beam Dia. (cm)	15	1.2	3.3	2.2
Screen-Aperture Diameter (mm)	1.9	2.0	10	5.0
Accel-Aperture Diameter (mm)	1.4	2.0	10	5.0
Screen-Grid Thickness (mm)	0.38	0.51	1.5	0.51
Accel-Grid Thickness (mm)	0.51	0.51	1.5	0.51
Grid Spacing (mm)	0.51	0.51	3.8	1.9
Screen-Grid Open- Area Fraction (%)	67	54	67	67
Accel-Grid Open- Area Fraction (%)	34	54	67	67
Source-Neutral- Expansion Length [ℓ_s] (mm)	0.79	Not Computed	4.8	2.5
Source-Neutral Exit Fraction [F_s]	0.31	Not Computed	0.69	0.75
Grid Material	Mo	Mo	C	C

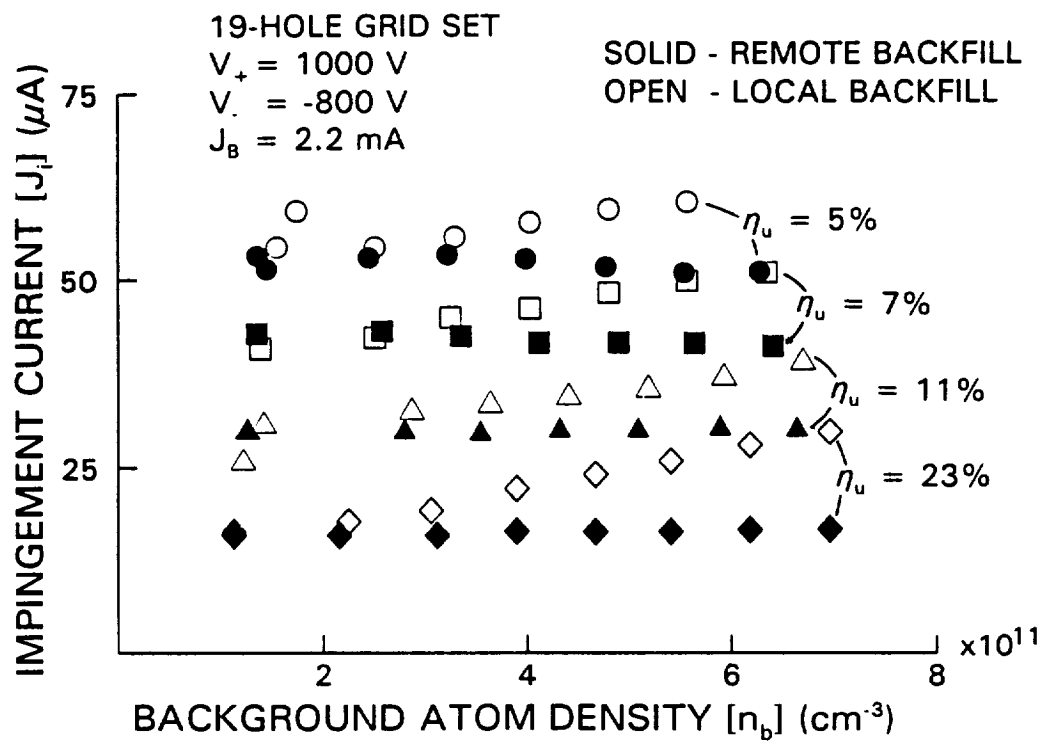
IV. Experimental Results

A. Verification of The Dominance of Charge-Exchange Ion Production

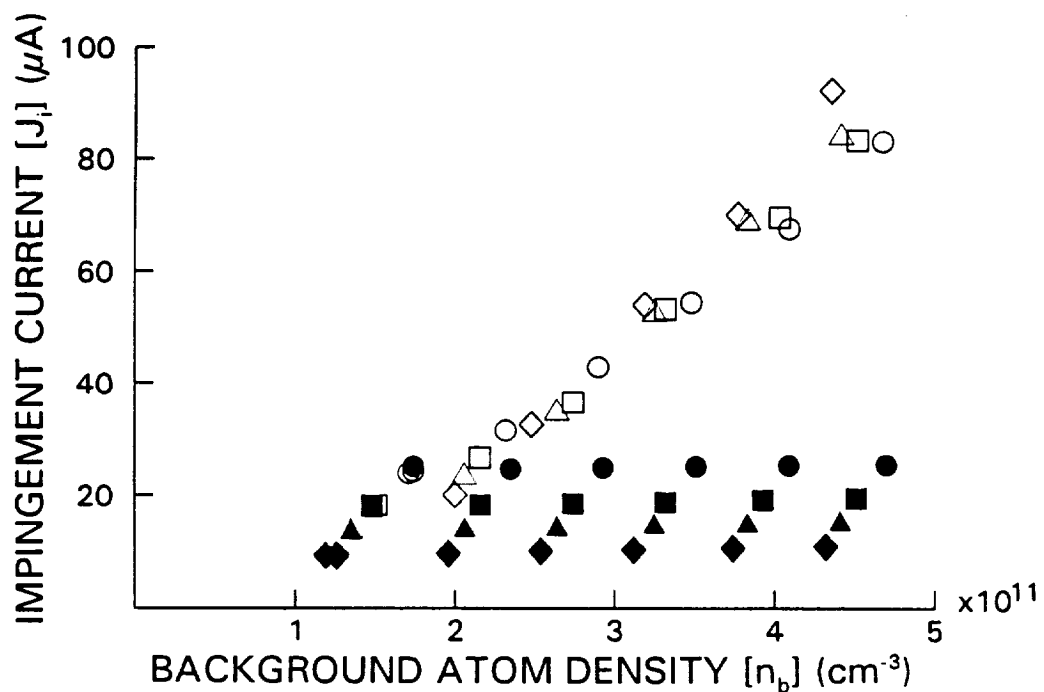
The simple, order-of-magnitude calculation (discussed in the theory section) suggested that the impingement current due to charge-exchange collisions is approximately 14 times greater than the current created by electron-impact ionization. In order to verify this result, the relative contributions of charge-exchange and electron-impact ionization to the total impingement current were also studied experimentally. The experiment involved measuring changes in impingement current as the background-atom density was increased by introducing either xenon or argon as a backfill gas into the vacuum chamber. Different species were used for the thruster propellant and backfill gas because the charge-exchange cross-section between ions of one species and atoms of another is approximately three orders-of-magnitude smaller than the cross-section for ions and atoms of the same species [17]. The electron-impact ionization cross-sections for xenon and argon, however, differ by only a factor of two or three [20]. Thus, any changes in the impingement current induced by increasing the background density via backfilling with the dissimilar species should be due to electron-impact ionization of this species and not charge-exchange. The changes in the impingement current were measured using the SERT II thruster

equipped with the 19-hole grid set and operated at a screen-grid potential (V_+) of 1000 V, an accel-grid potential (V_-) of -800 V, and a constant beam current (J_B) of 2.2 mA.

The results of Fig. 9a were obtained when xenon was introduced into the thruster (the propellant) while argon, which was the backfill gas, was introduced either locally (near the accel grid) or remotely (2.7 m downstream of the accel grid) to increase the background-atom density. These data show the effects of changes in the measured impingement current as the background atom density and propellant utilization (accomplished by increasing the thruster flow rate at a constant beam current) are changed. They reveal that remote introduction of argon (solid symbols) causes negligible changes in the impingement current, however, local introduction of argon (open symbols) causes the impingement current to increase from 12 to 25 μA for a propellant utilization of 23%. Similar trends in the impingement current data are shown for propellant utilizations of 11, 7, and 5%. Currently, these slight increases in the impingement current as the argon is introduced locally are believed to be due to modest argon ingestion, its subsequent ionization within the thruster, and its extraction as a small fraction of the beam current that does charge-exchange with the argon backfill. The data of Fig. 9a also show that changes in the propellant utilization cause the greatest change in the impingement current. For example, at a density of $1 \times 10^{11} \text{ cm}^{-3}$ increasing the propellant utilization from 5 to 23% causes the impingement current to decrease by 400%. Considering only three sources for neutral atoms (the discharge chamber, the local backfill, and the remote backfill) this



a) Xe Propellant, Ar Backfill



b) Ar Propellant, Xe Backfill

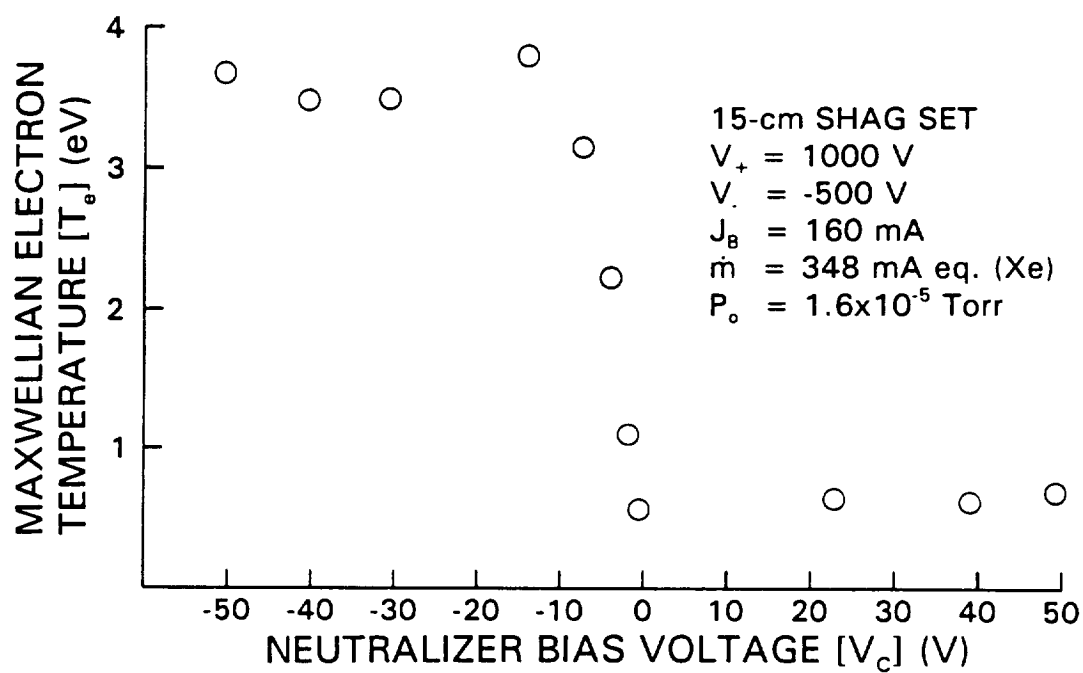
Fig. 9 Background-Atom-Density Effects on Impingement Current

data trend suggests that charge-exchange between the xenon beam ions and xenon propellant atoms from the discharge chamber (whose density is determined by the propellant utilization) dominates the production of impingement-current ions. This, along with the relative insensitivity of the impingement current to the argon background density further supports the conclusion that charge-exchange is the dominate impingement-current ion production mechanism.

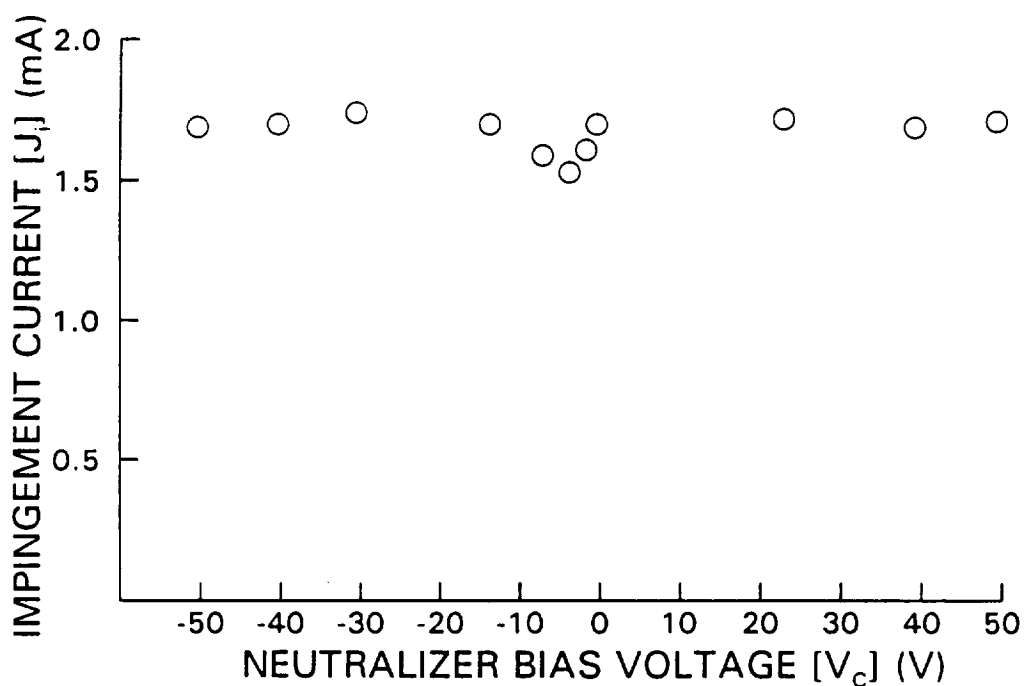
The impingement-current-v.-background-atom-density data obtained using argon as the propellant and xenon as the backfill gas are presented on Fig. 9b. In this case, the solid symbols show a slight increase in impingement current as xenon is remotely backfilled. These data, similar to the data of Fig. 9a, show that changes in the propellant utilization have a greater effect on the impingement current than do changes in the background density when xenon is remotely backfilled. The open symbols, however, show a great impingement-current sensitivity to local xenon backfill. Two reasons for this increased sensitivity are postulated. First, when xenon is introduced locally the thruster ingests a significant amount of it and since the discharge voltage is higher for a thruster operating on argon, this ingested xenon is ionized readily and contributes substantially to the extracted ion beam current. These xenon beam ions can then charge-exchange with the backfilled xenon atoms and cause the observed increase in impingement current. This mechanism is supported by an observed decrease in the discharge voltage to a value similar to that for thrusters operating on xenon as the background-xenon density is increased.

A second possible reason for the dramatic increase in impingement current

when xenon is backfilled locally is related to the lower ionization potential for xenon (12.13 eV as compared to 15.76 eV for argon). This would enable thermalized (Maxwellian) electrons in Region 4 to ionize the xenon backfill more readily than argon. To determine if Maxwellian-electron-impact ionization could be causing the observed difference between the xenon and argon backfill cases, the impingement current was measured as the Maxwellian temperature of the beam plasma was increased while the thruster was operating on xenon. To obtain the required data, the SERT II thruster was equipped with the 15-cm-SHAG set, operated at the conditions presented in the legend of Fig. 10, and the spherical-Langmuir probe was used to measure the ambient-plasma-Maxwellian-electron temperature. The neutralizer-bias voltage was swept from -50 to 50 V to induce the temperature change, and the electron-temperature data presented on Fig. 10a were measured 1 cm downstream from the accel-grid on the thruster centerline. These data show that positive neutralizer bias voltages induce electron temperatures of about 0.5 eV while negative bias voltages induce temperatures that are about 3.5 eV. This-three-electron volt change in temperature should induce a 10-order-of-magnitude increase in the electron-impact rate factor (the relative velocity/cross-section product). Assuming that the other plasma properties remain constant (i.e., the neutral and electron densities), such a large increase in the rate factor should induce a gigantic increase in the impingement current. The data of Fig. 10b, however, show that the impingement current remained almost constant at 1.6 mA as the neutralizer-bias voltage was swept from -50 to 50 V. Thus from the data of Figs. 9 and 10 it can be concluded that



a) Maxwellian Electron Temperature



b) Impingement Current

Fig. 10 Effects of Neutralizer Bias Voltage on Maxwellian Electron Temperature and Impingement Current

electron-impact-ionization does not contribute significantly to the production of impingement-current ions.

B. Determination of the Differential-Impingement-Current-Integral Limits

The emissive probe was used to measure the potential field downstream of the accel grids used in this study and from these data the length of Region 3 could be determined. A typical centerline potential profile obtained using the IPT is presented on Fig. 11 along with the SERT II thruster operating conditions and axial positions of both the screen and accel grids. The circles show that upstream of the accel-grid surface (the intra-grid region where axial positions are negative), the potential is positive and as the probe moves slightly downstream the potential decreases dramatically from 75 to -250 V. For axial positions greater than 0 cm the potential increases from the minimum of -250 to a value just negative of ground for positions greater than 0.5 cm. Based on this potential profile it can be concluded that all charge-exchange ions created between the downstream surface of the accel grid and an axial position of ~ 0.5 cm will impinge upon the grid. This suggests that ℓ_3 is ~ 0.5 cm for these operating conditions. In addition, these data suggest that a very slight centerline-potential peak may be located near ℓ_3 .

While using the IPT method to collect the data of Fig. 11 two interesting phenomena were observed. First, when the emissive probe was located within the ambient plasma (axial positions greater than 0.5 cm for the data of Fig. 11), decreasing its bias more negative than about -250 V (the minimum potential of

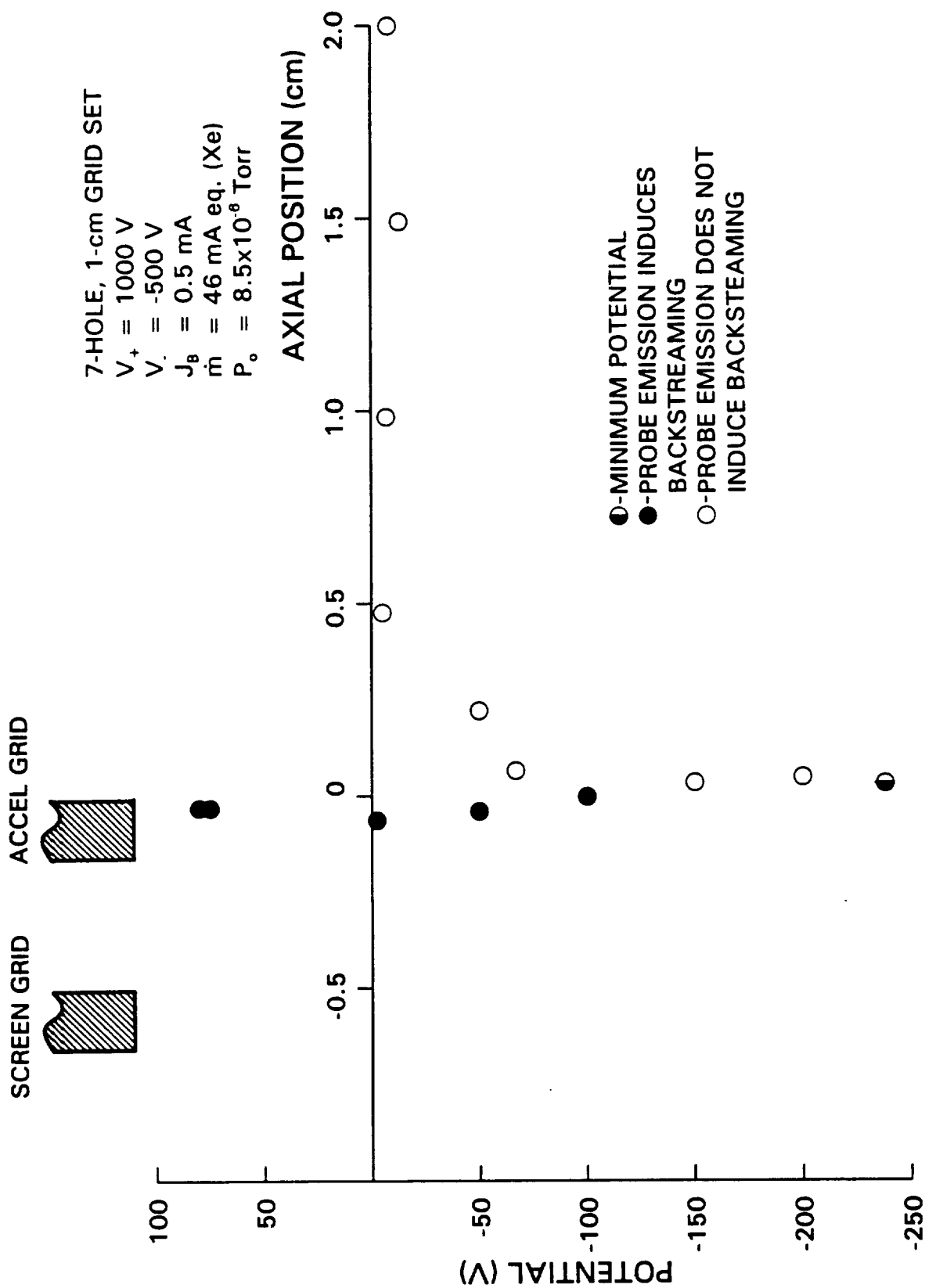


Fig. 11 Typical Centerline Potential Profile

Fig. 11) caused an increase in the apparent beam current. It appears that this occurred because electrons emitted from the probe had sufficient energy to get through the grids and into the discharge chamber (electron backstreaming). This suggests that the minimum-centerline potential (termed the saddle-point potential and indicated on Fig. 11 by the half-solid circle) can be determined by placing an emissive probe within the ambient plasma, biasing it to increasingly negative potentials and then recording the saddle-point potential where the beam current begins to increase due to backstreaming. The second phenomena observed while using the IPT is that an emissive probe located upstream of the saddle-point-potential axial position will emit electrons readily to the ion thruster when its potential is more negative than the local potential. In contrast, a probe located downstream of the saddle-point axial position biased slightly negative of the local potential will not cause the electrons emitted from the probe to be collected by the thruster. The axial positions at which the filament emission current affects the beam current for the experiment associated with Fig. 11 are shown by the solid symbols and those positions where the probe current has no affect on the beam current are shown by the open symbols.

To determine how radial potential gradients affect the measurement of ℓ_3 , the IPT was used to measure the local potential variation as a function of both radial and axial position for a plane passing through the grid-set centerline. The equi-potential-surface plot measured for the thruster equipped with the 7-hole, 1-cm grid set and operated at the conditions given on the legend is presented as Fig. 12. This map

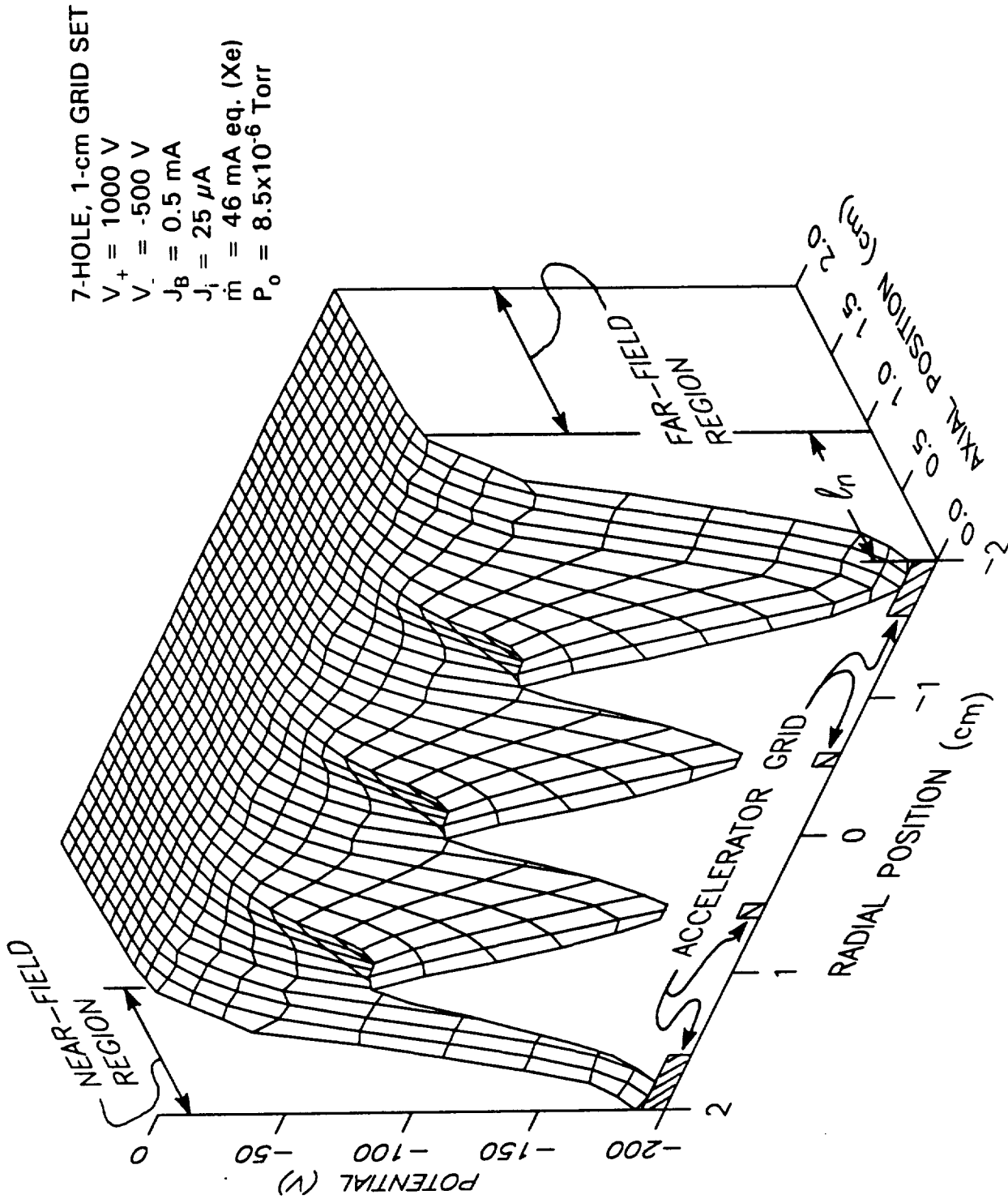


Fig. 12 Typical Downstream, Equi-Potential Surface Map for the 7-Hole, 1-cm Grid Set

shows three distinct potential peaks created by individual ion beamlets (at axial positions between 0 and 0.5 cm and radial positions of 0 and ± 1.1 cm, respectively). Also shown are two distinct potential-gradient regions called the near- and far-field regions. The strong axial and radial potential gradients near the downstream face of the accel grid (shown cross-hatched) define the near-field region. Within the far-field (ambient plasma) region, on the other hand, the potential gradients are too weak to be seen. The distance from the accel grid to the boundary between the near- and far-field regions is defined as the neutralization length (ℓ_n) because electrons from the far-field region that reach this boundary are reflected back downstream. Essentially no electrons will be present within the near-field region. Data presented on Fig. 12 also indicate that all charge-exchange ions produced in the near-field region ($0 \leq z \leq \ell_n$) will impinge on the accel grid and contribute to the impingement current and sputter erosion. This leads to the conclusion that the length of Region 3 (ℓ_3) is equal the neutralization length (ℓ_n) identified on Fig. 12.

The strong, radial potential-gradients that are apparent in the near-field region shown of Fig. 12 will tend to accelerate charge-exchange ions produced within the beamlets (the potential crests) radially into the potential troughs located between the beamlets. The axial components of these gradients will, on the other hand, accelerate them upstream into the accel grid (primarily into the centroid of the triangular shaped region formed by three grid apertures). These acceleration processes should produce erosion patterns that are consistent with those found on the downstream surfaces of many accel grids [13,30,10].

A careful examination of the Fig. 12 reveals that only very slight potential peaks (barriers to upstream ion flow) exist at ℓ_n near the centerline of the individual beamlets. At first glance it may seem that they might prevent charge-exchange ions created in the far-field (ambient) plasma from migrating upstream of ℓ_n and impinging on the accel grid. Closer examination shows, however, that these individual potential barriers do not represent a continuous potential ridge across the entire ion beam; thus it is possible for charge-exchange ions created in the far-field region to pass between adjacent peaks and impinge on the accel grid. The lack of a continuous downstream-potential peak implies that accurate calculation of the impingement current must include charge-exchange ion production within both Regions 3 (the near-field region) and 5 (the far-field region/ambient plasma). Hence all of the terms in the source- and background-dominated expressions developed to describe the impingement current due to charge-exchange ions (Eq. 22) should be used to compute these currents.

An equi-potential surface map was also obtained for the plasma region downstream of the SERT II ion thruster equipped with the 15-cm SHAG set and operated at the conditions presented on Fig. 13. This map, which was obtained on a much larger scale than Fig. 12, does not show the presence of individual ion beamlets. The figure does show, however, that even for this large-beam-diameter grid set there is no downstream potential-ridge that would be expected to prevent charge-exchange ions produced in the ambient plasma from contributing to the impingement current. The map, also suggests that large-scale, radial potential gradients are weak over the central region of the ion beam (about ± 7.5 cm) so the

15-cm SHAG SET
 $V_+ = 1000 \text{ V}$
 $V_- = -500 \text{ V}$
 $J_B = 420 \text{ mA}$
 $J_i = 4.0 \text{ mA}$
 $\dot{m} = 500 \text{ mA eq. (Xe)}$
 $P_o = 2.3 \times 10^{-5} \text{ Torr}$

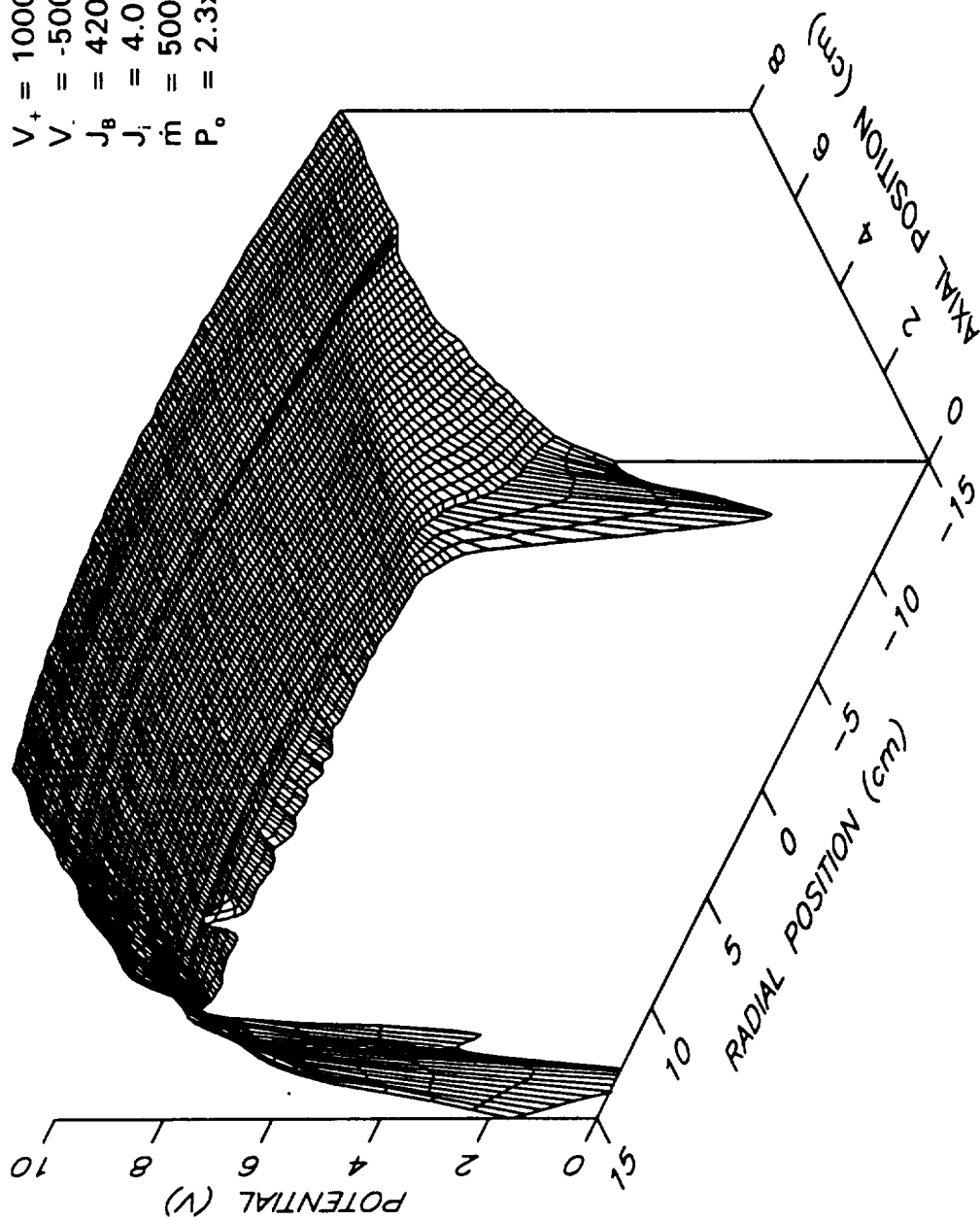


Fig. 13 Typical Downstream, Equi-Potential Surface Map for the 15-cm SHAG Set

one-dimensional model developed should accurately predict impingement currents associated with this large-diameter ion beam.

The final observation to make about the data of Fig. 13 is that there is a large potential trough at the beam periphery. At an axial position near zero, the potentials associated with this trough decrease from the uniform beam plasma potential of 8 V to ~ 0.2 V and then increases to ~ 6 V at radial positions significantly outside the ion beam. This potential-trough structure around the beam extends axially downstream for several centimeters and can be expected to focus charge-exchange ions produced several centimeters downstream into a relatively narrow band around the active-beam-extraction area of the accel grid. This potential structure and charge-exchange-ion-acceleration process it induces may explain the narrow erosion ring observed in the grid failure documented by Brophy [33].

C. Neutralization-Length Measurements

The neutralization length (ℓ_n) can be measured from potential data similar to those presented on Fig. 12, however it is desirable to make this measurement using a method other than the IPT method of data acquisition because this method is very time consuming. For example, to obtain a potential map from which ℓ_n can be measured, the emissive probe is positioned at a discrete axial and radial position, current/voltage data are collected and then later analyzed to yield the local potential at that location. This procedure must be repeated for several axial and radial positions until a sufficient number of potentials have been measured and plotted from this plot

ℓ_n can be obtained. To find a more time efficient method of making this measurement, the effects of beamlet ion charging on the floating potential of the hot-filament emissive probe were investigated. The details are described in Appendix A but the work can be summarized by noting that floating potential measured using an emissive probe were compared to potentials measured using the IPT when the thruster was operated with the 7-hole, 1-cm grid set. A typical comparison of floating- and IPT-potentials profiles is shown on Fig. 14 and the data show that the floating potential data (the solid line) differs greatly from those obtained using the IPT (the circles) upstream of 0.75 cm. However, the floating and inflection-point data agree to within a few volts of the inflection point data in the ambient plasma region downstream of 0.75 cm. Most importantly though, both sets of data show a decrease in potential at 0.6 cm (labeled the floating-potential break-point). This agreement suggests that either method can be used to measure the distance from this point to the accel grid (the neutralization length). This is an important result for this study because it shows that ℓ_n can be measured using the relatively simple procedure of measuring the axial variation of the floating potential and then identifying the location at which the slope changes from near zero to a positive value.

Values for ℓ_n (measured using the floating-potential procedure) have been obtained and compared to those computed using the Kerslake model (Eq. 24) over a wide range of operating conditions. The effects of varying the beam current from 0.25 to 3.75 mA on ℓ_n are presented on Fig. 15 along with the thruster operating and configuration conditions. The experimental values for ℓ_n are shown by the circular

7-HOLE, 1-cm GRID SET
 $V_+ = 1000 \text{ V}$
 $V_- = -500 \text{ V}$
 $J_B = 3.0 \text{ mA}$

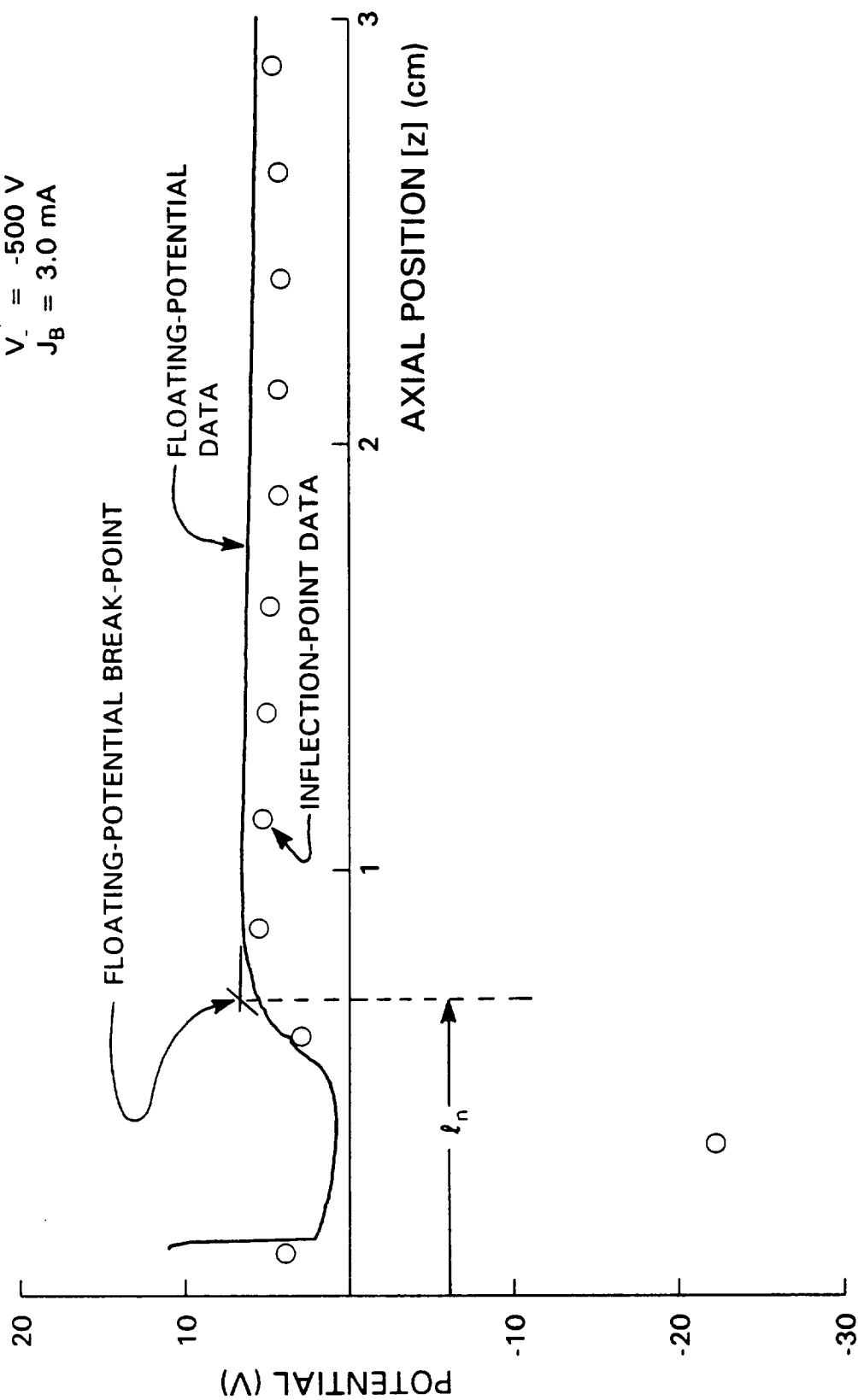


Fig. 14 A Comparison of Inflection-Point and Floating-Potential Data

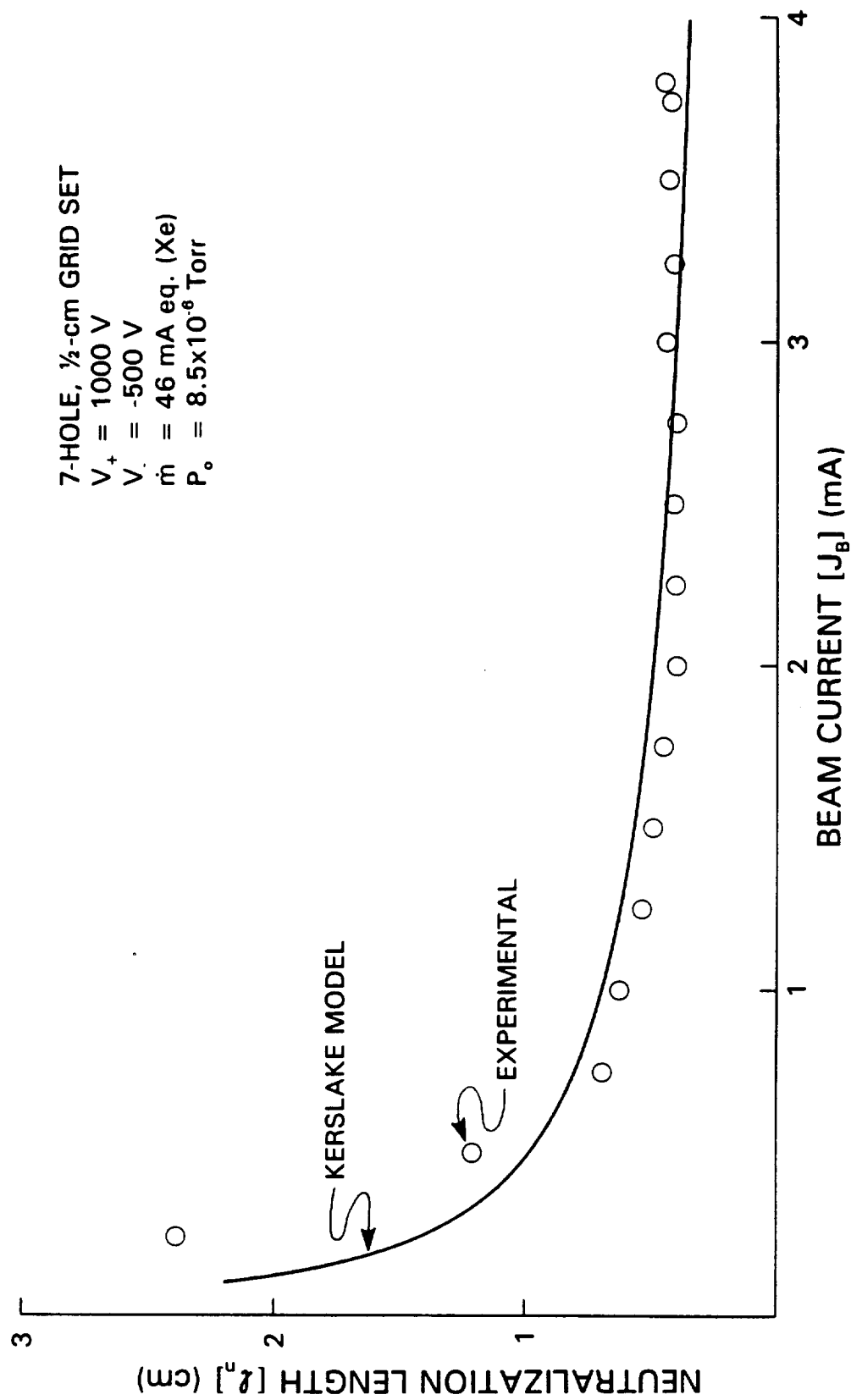


Fig. 15 Effects of Beam Current on ℓ_n

data points while the solid line represents those computed using the Kerslake model. These experimental data show that ℓ_n decreases rapidly from 2.5 to 0.75 cm as the beam current increases from 0.25 to 1 mA and for beam currents greater than 1.5 mA, ℓ_n remains relatively constant near 0.5 cm. A comparison between the experimental and calculated values for ℓ_n show that both agree very well over the entire beam-current range investigated.

The effects of varying the screen-grid potential over the range from 600 to 1600 V, on ℓ_n , are presented on Fig. 16. Again the circular data points are the experimentally measured values for ℓ_n and the solid line represents the values computed using the Kerslake model. There is some scatter in the experimental data shown; in general, however, they bound the predicted values, which exhibit a slight increase with screen-grid potential. Similar data showing the effect of increasing the accel-grid potential from -1600 to -300 V on ℓ_n are presented on Fig. 17. These experimental data show that as the accel-grid potential is increased, ℓ_n decreases linearly from ~ 1.25 to 0.25 cm. Results computed using the Kerslake model also show a decrease in ℓ_n with increasing accel-grid potential, however, the curve has a slight curvature and a less-negative slope than the experimental data. Both data sets do, however, predict ℓ_n values that are of comparable magnitudes, so the agreement between them is considered good.

The effect of changes in the ambient xenon density on ℓ_n was determined by operating the thruster at a constant condition (given on Fig. 18) and increasing the background-atom density by introducing xenon 2.7 m downstream from the thruster.

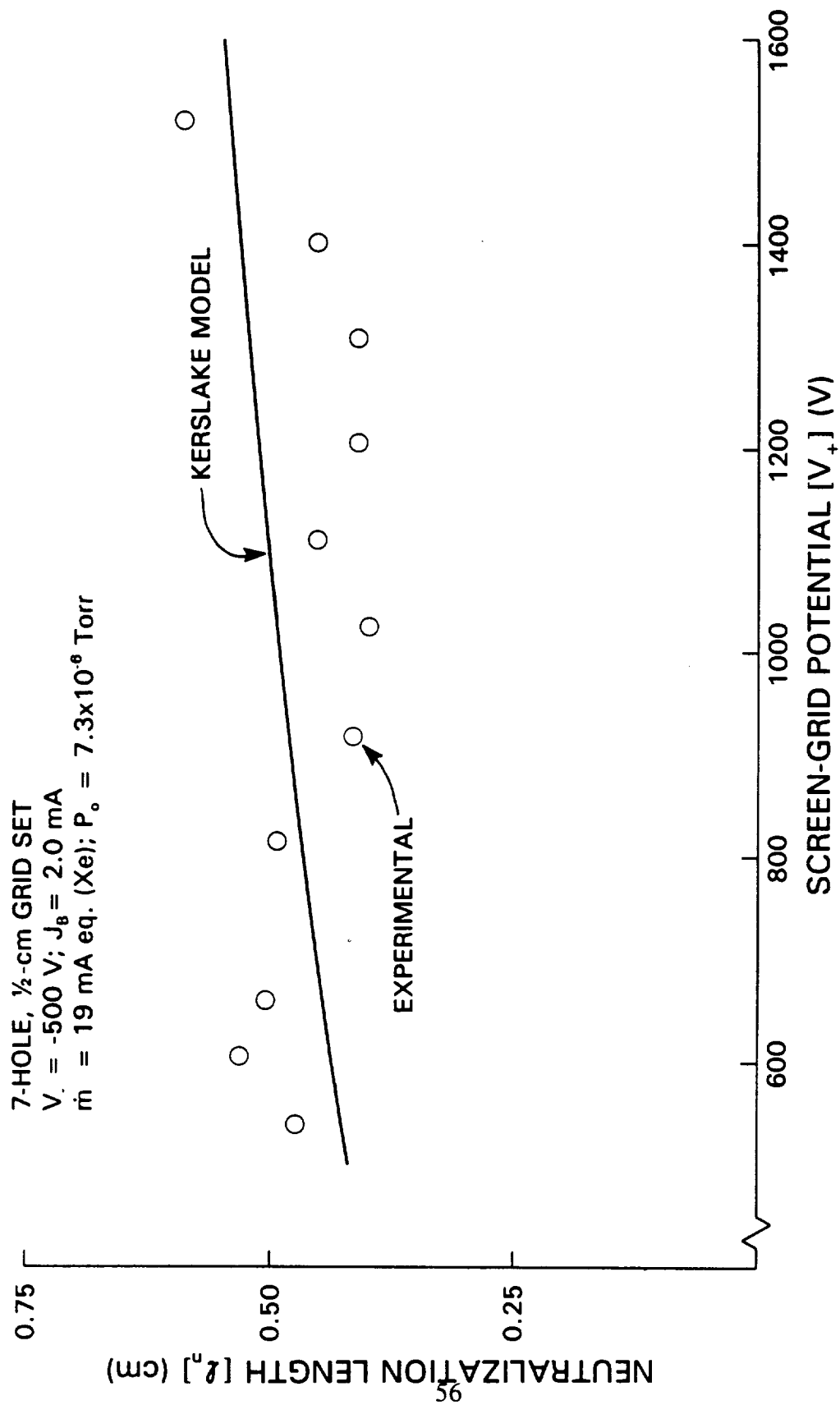


Fig. 16 Effects of Screen-Grid Potential on l_n

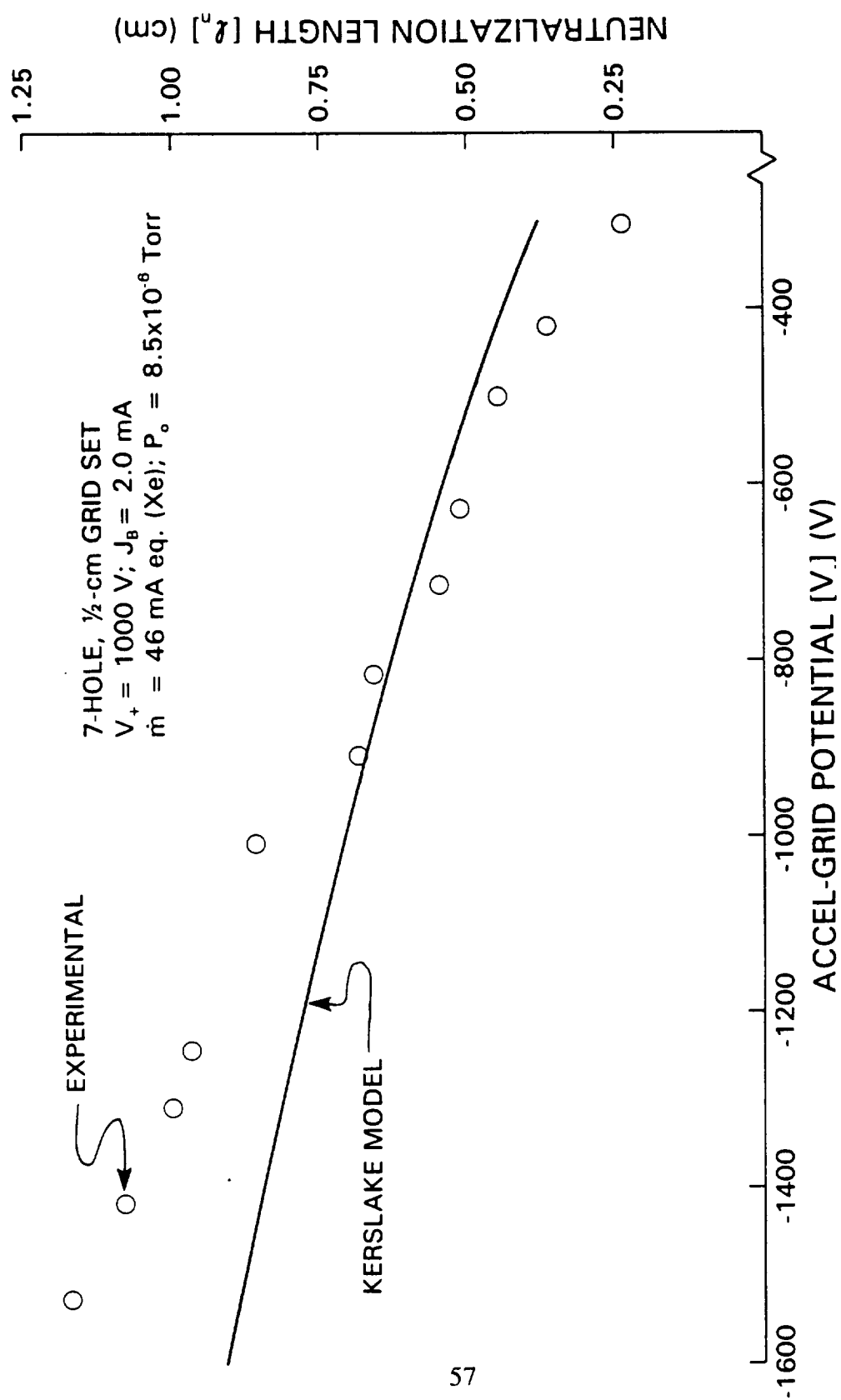


Fig. 17 Effects of Accel-Grid Potential on ℓ_n

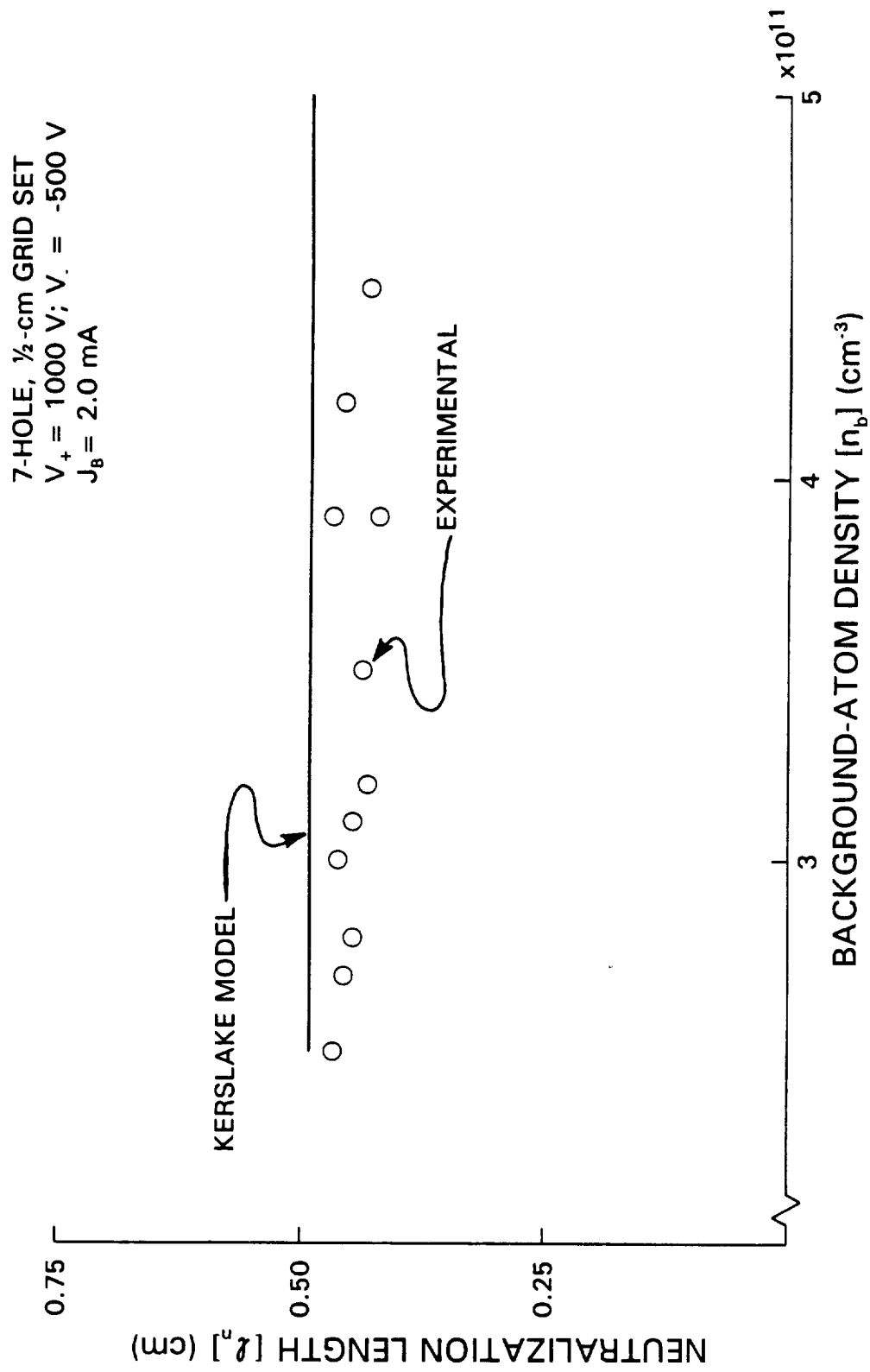


Fig. 18 Effects of Background-Atom Density on ℓ_n

The circular data points on the figure show that increasing the density from 2.5×10^{11} to $4.5 \times 10^{11} \text{ cm}^{-3}$ induces no significant change in ℓ_n . The mean value from the experiments (0.48 cm) agrees well with the constant value (0.49 cm) predicted by the Kerslake model.

Experiments were also performed to determine the effects of variations in neutralizer-bias voltage and keeper current on ℓ_n . The experimental (circular points) and predicted values (solid line) showing the effects of the neutralizer-bias voltage, varied from -10 to 10 V, on ℓ_n are given in Fig. 19 for the thruster operating at the conditions indicated there. Figure 19 shows that the neutralizer-bias voltage affected neither the measured or computed values for ℓ_n , which remained constant at ~ 0.42 and 0.49 cm, respectively. Similarly, the data of Fig. 20 show that increasing the neutralizer-keeper current from 300 to 1200 mA, has no effect on either the measured (the circular data points) or the Kerslake-model values (the solid line) for ℓ_n . These data again suggest that at these thruster conditions the experimental and Kerslake values for ℓ_n agree quite well.

The data of Figs. 15-20 show that of the thruster and neutralizer operating parameters investigated only the beam current, screen-grid and accel-grid potentials affect ℓ_n . However, no data have been presented to show how changes in the grid-set geometry effect this length. The fact that beam currents extracted from and the intra-grid spacings for the 7-hole-grid and SHAG sets differ by orders of magnitude suggests that some parametric normalization will be required before such a comparison between experimental and theoretical data can be made. The appropriate

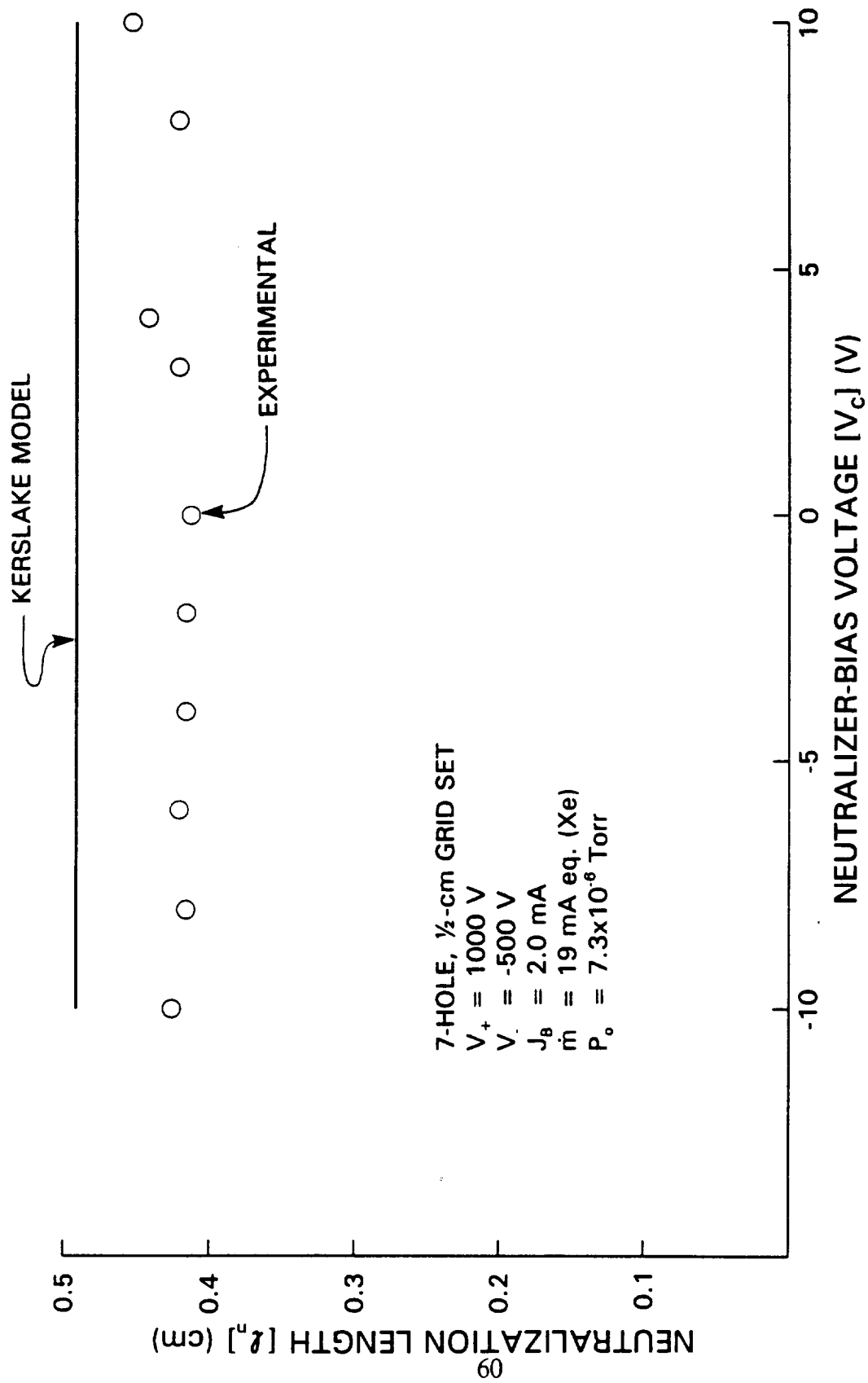


Fig. 19 Effects of Neutralizer-Bias Voltage on ℓ_n

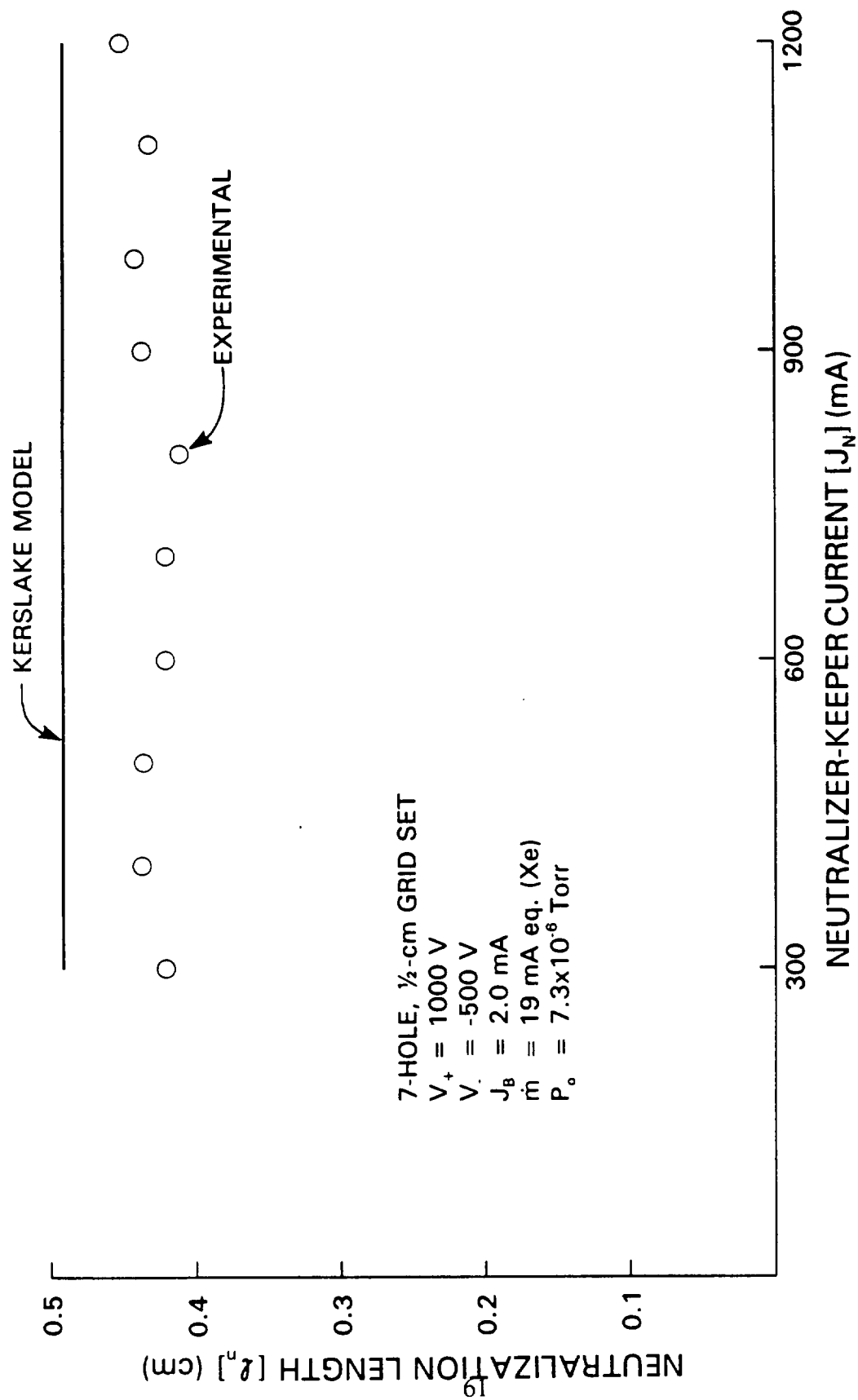


Fig. 20 Effects of Neutralizer-Keeper Current on l_n

parameters for the comparison are those developed in Section II.E, namely the normalized perveance-per-hole (P - Eq. 26) and the non-dimensional-neutralization length ($\tilde{\ell}_n = \ell_n/\ell_c$ where ℓ_c is defined by Eq. 27). Experimental data obtained for the 1) 7-hole, $\frac{1}{2}$ -cm-grid set (the circular data points), 2) 7-hole, 1-cm-grid set (the square points), and 3) 15-cm SHAG set (triangular data points) are presented on Fig. 21 along with the Kerslake values (the solid line, Eq. 28). This figure shows that the circular data points agree very well with the predicted values over the entire perveance range investigated, the square data points agree well for perveance values above 0.5, and the triangles agree for perveance values below ~ 0.2 . In general, however, all the data presented agree fairly well with the predicted values for $\tilde{\ell}_n$.

The use of $\tilde{\ell}_n$ and normalized perveance-per-hole for a comparison between experimental and theoretical ℓ_n data obtained for the three grid sets as either the screen- or accel-grid potentials vary becomes inconvenient because both the normalized perveance-per-hole and the net-to-total voltage ratio (R) vary. To eliminate this inconvenience, both sides of Eq. 24 were multiplied by the square root of the beamlet-current density which was approximated as the beamlet current divided by the beamlet area. This operation eliminates the dependence of the Kerslake model on beam current and grid-set geometries allowing a direct comparison between data obtained using the three grid sets. The effects of varying the screen-grid potential from 500 to 1600 V, at a constant accel-grid potential of -500 V, on this parameter are presented on Fig. 22 for the two 7-hole-grid and the SHAG sets. The circular points correspond to the 7-hole, $\frac{1}{2}$ -cm-grid data, the squares to the 7-hole, 1-cm data,

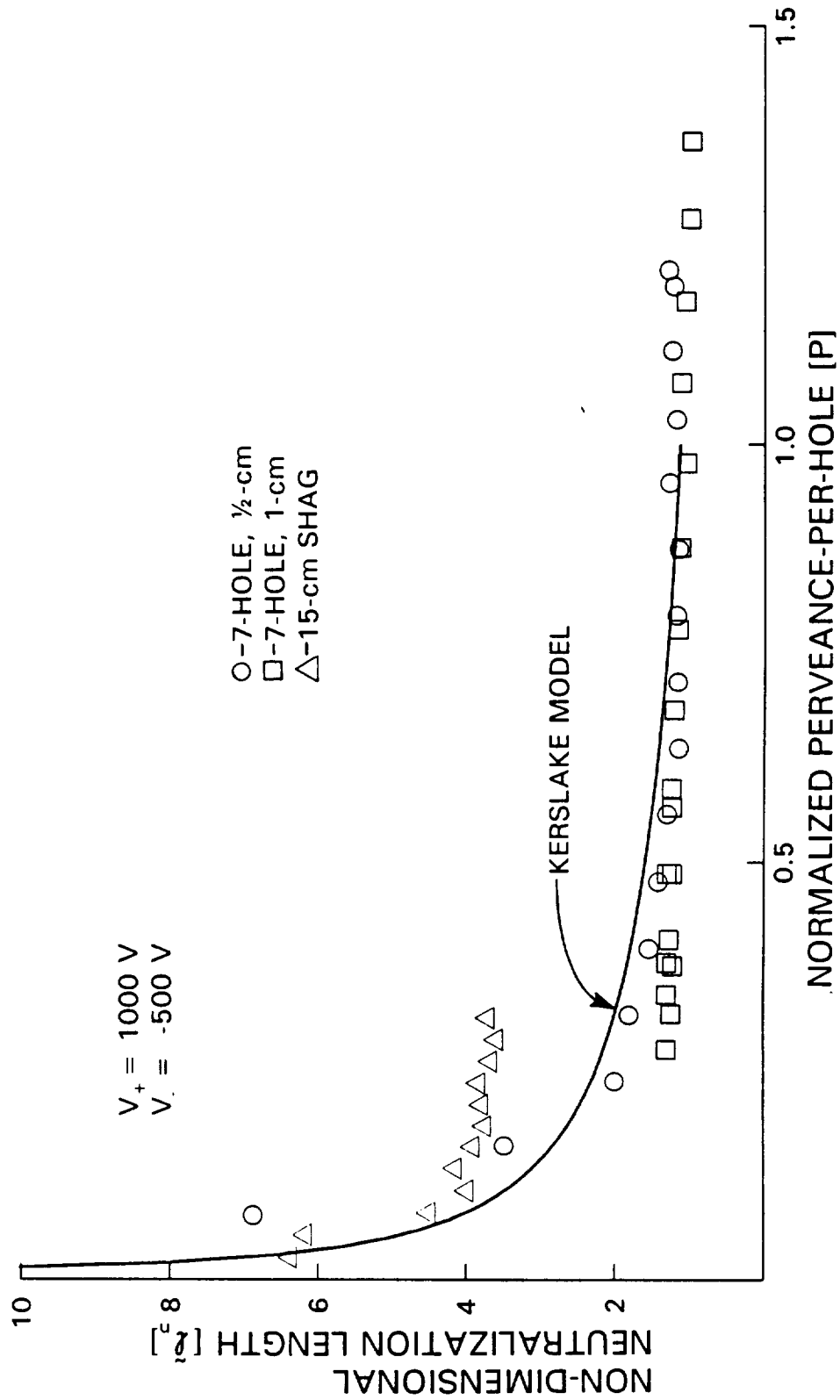


Fig. 21 Comparison of \bar{L}_n Data Obtained on the 7-hole-Grid and SHAG Sets

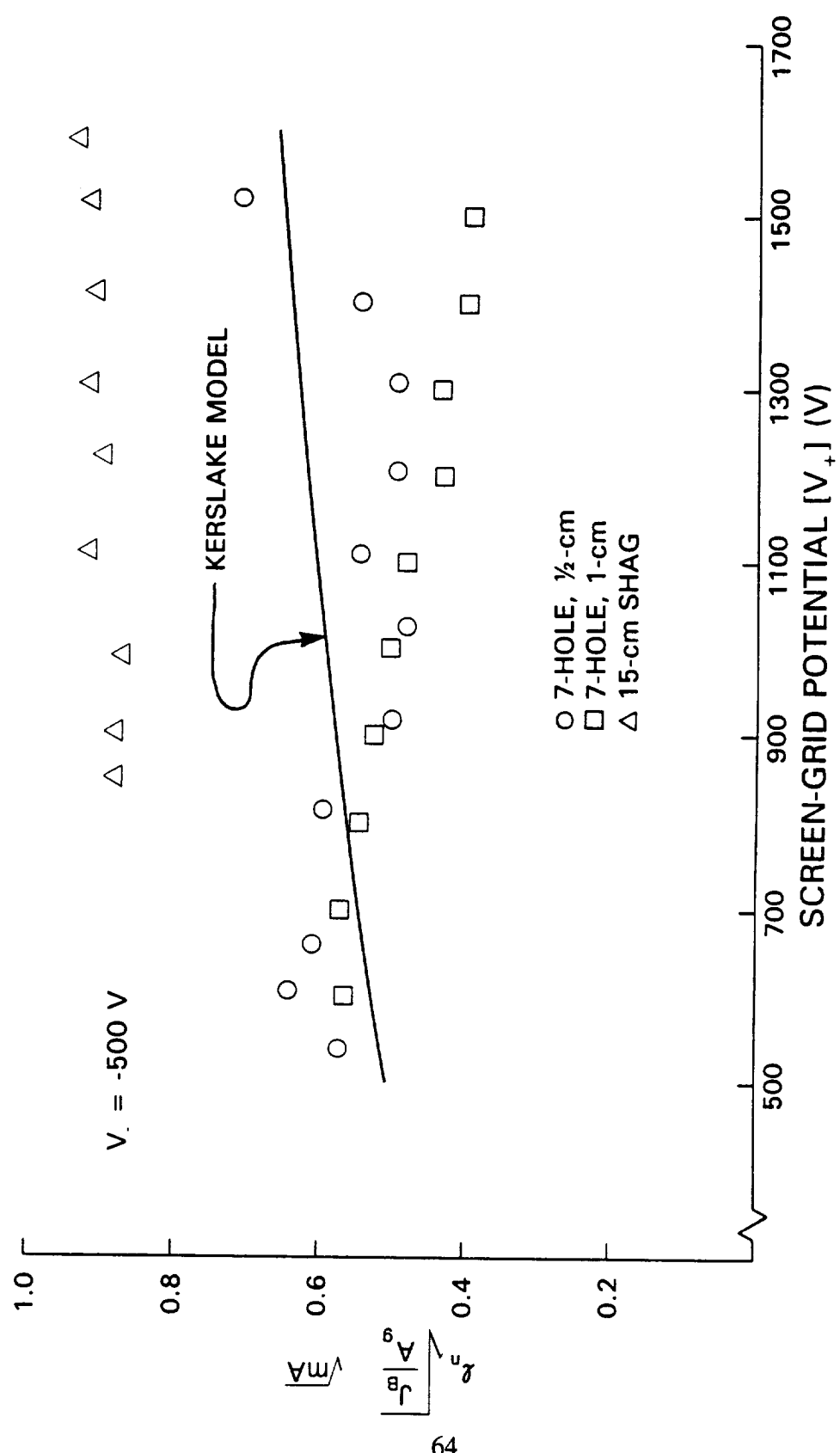


Fig. 22 A Comparison Between Measured and Predicted Effects on Changes in the Screen-Grid Potential

the triangles to the SHAG set and the solid line to the predicted data. This figure shows that the experimental data for the 7-hole-grid sets compares well in magnitude but not in trend with the predicted values and the 15-cm-SHAG data agree well in trend but not in magnitude.

Presented on Fig. 23 are the effects of varying the accel-grid potential from -1600 to -300 V at a constant screen grid potential of 1000 V. Again the circles are the 7-hole, $\frac{1}{2}$ -cm data, the squares are the 7-hole, 1-cm data, the triangles are the 15-cm-SHAG data and the solid line represents the predicted values. This figure shows that all the experimental data follow similar trends as the accel potential is varied over the aforementioned range. The SHAG data and the 7-hole, $\frac{1}{2}$ -cm data at very negative grid potentials are, however, 30 to 50% greater than the values predicted by the Kerslake model.

D. A Comparison Between Experimental and Computed Impingement Currents

All the data presented in the proceeding section have shown the effects of varying thruster and neutralizer operational parameters and grid-set geometries on ℓ_n . It is, however, the effect of these parameters on the measured impingement current and the agreement between this current and the computed current (Eq. 22) that is of primary interest. Figure 24 is a comparative plot showing the measured and computed impingement currents as a function of beam current for the SERT II ion thruster operating at the conditions given on the figure. The open, circular data

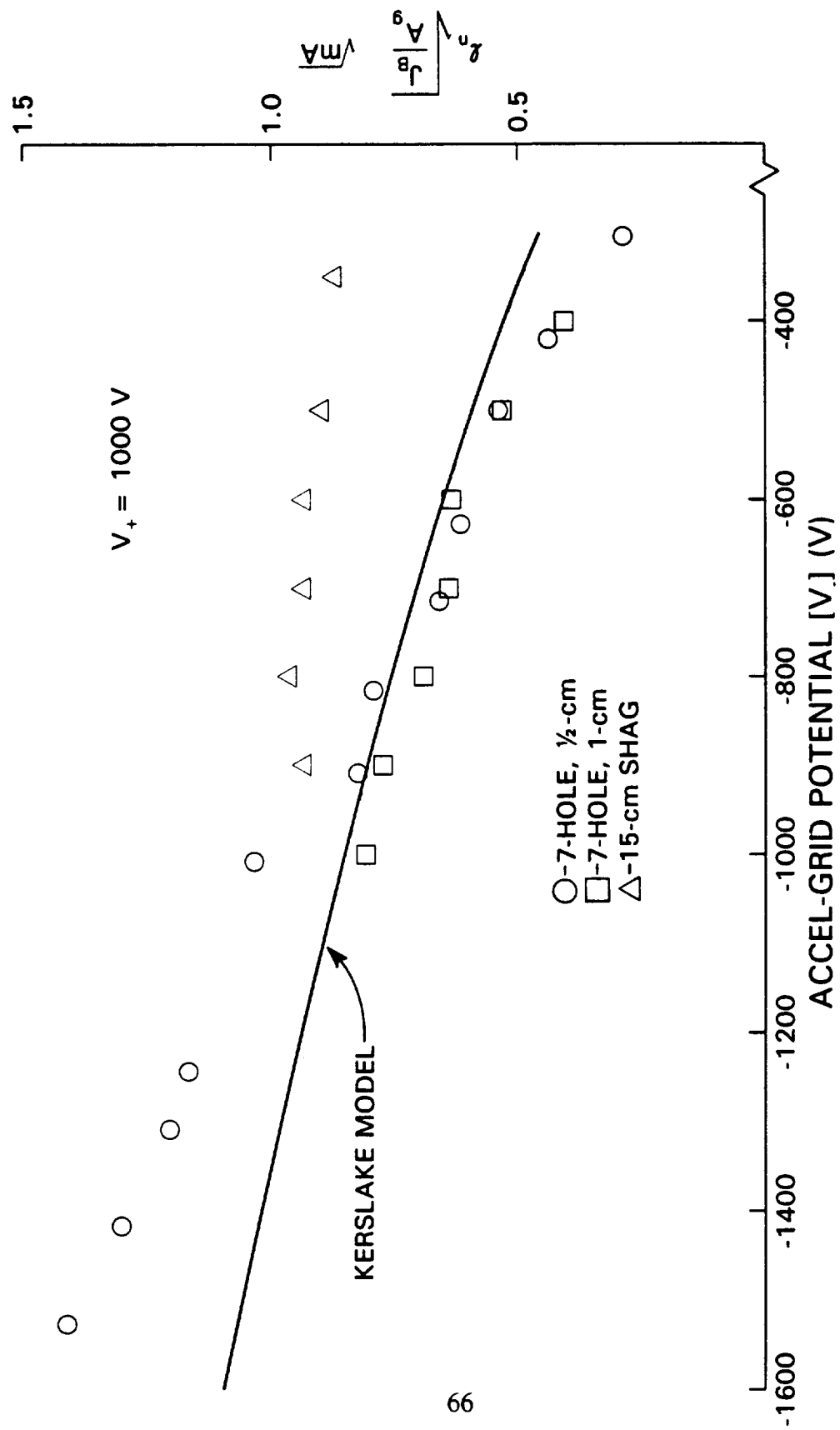


Fig. 23 A Comparison Between Measured and Predicted Effects on Changes in the Accel-Grid Potential

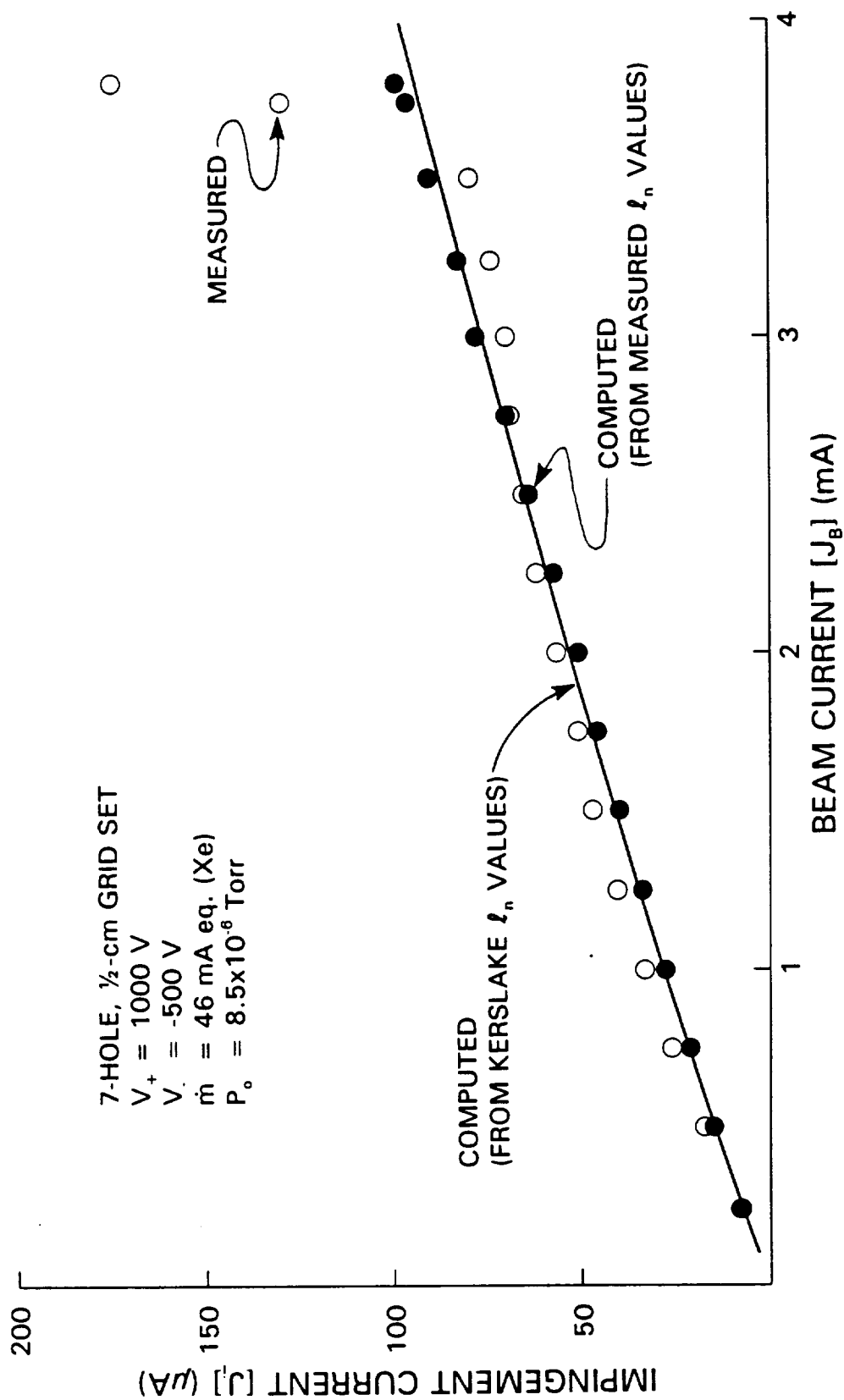


Fig. 24 Effects of Beam Current on Impingement Current for the 7-hole, 1/2-cm Grid Set

points show that as the beam current increases from 0 to 3.5 mA the measured impingement current increases linearly from 0 to 60 μA . Further increases in the beam current cause direct impingement of the beamlet ions (shown by the dramatic increase in the measured impingement current at high beam currents). The solid circles presented on the figure are the computed impingement currents obtained using the measured values of ℓ_n (taken from Fig. 15) and they show excellent agreement with the measured currents below the onset of direct impingement. The solid line presented on Fig. 24 is the impingement current computed using the Kerslake-model values for ℓ_n and as expected this line agrees very well with both the solid circles and the open circles below the onset of direct impingement. This excellent agreement between the two computed impingement currents is not surprising because the data of Fig. 15 show excellent agreement between the measured and calculated ℓ_n values.

The effects of varying the screen-grid potential on the measured and computed impingement currents are presented on Fig. 25 along with the thruster operating conditions. This figure shows that the impingement currents computed using both the measured and Kerslake values for ℓ_n (solid circles and solid line) show excellent agreement with each other, and they are 50% greater than the measured currents (open circles) at a screen-grid potential of 500 and drop to 25% below the measured values as this potential reaches ~ 1600 V. Measured and computed impingement currents obtained as the accel-grid potential was increased from -1600 to -300 V are given on Fig. 26 along with the thruster operating conditions. This figure shows that both computed impingement currents (solid circles and line) agree well with each

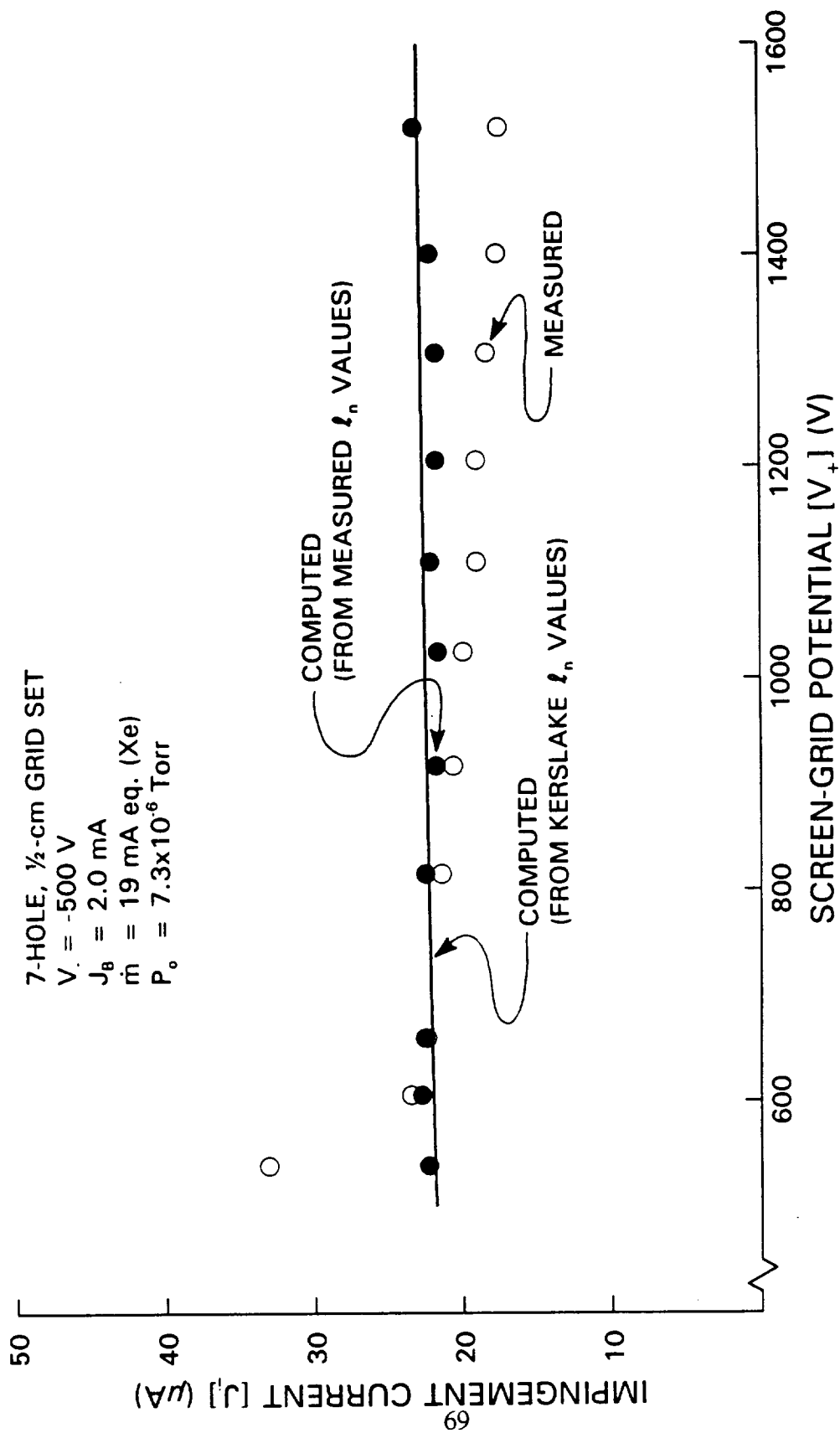


Fig. 25 Effects of Screen-Grid Potential on Impingement Current for the 7-hole, 1/2-cm Grid Set

other except at accel-grid potentials near ~ -400 V where the solid circles are 10 to 20% below the solid line. The figure also shows that these computed currents are fairly constant over the accel-grid potential range investigated and are from 30% greater to 30% smaller at potentials of -1600 V and -300 V, respectively. The effects of increasing the background-atom density from 2×10^{11} to 4.5×10^{11} cm^{-3} on the measured and computed impingement currents are presented on Fig. 27. The figure shows that the agreement among the three impingement currents is very good at the low background-densities. As the background density increases, however, the computed impingement currents do not increase as rapidly as the measured ones do, so at a background density of 4.5×10^{11} cm^{-3} the measured impingement current is 20% greater than the computed values.

The data presented on Figs. 24-27 show that the 1-D theory for predicting impingement currents calculates values that generally agree with measured values to within $\sim 20\%$ as the beam current, screen- and accel-grid potentials, and background-atom densities for the 7-hole, $\frac{1}{2}$ -cm grid set are varied. There are, however, a few points at extreme voltage conditions where the measured and computed results differ by as much as 50%. Similar data obtained using the 7-hole, 1-cm grid and the 15-cm SHAG sets (but not presented here) show similar behavior as thruster operating conditions and background atom density are varied although measured and computed impingement currents do not agree quite as well ($\pm 30\%$ is more typical for these grid sets). The effects of beam current on the measured and computed impingement currents for all three grid sets are shown in Figs. 24, 28 and 29. The impingement-

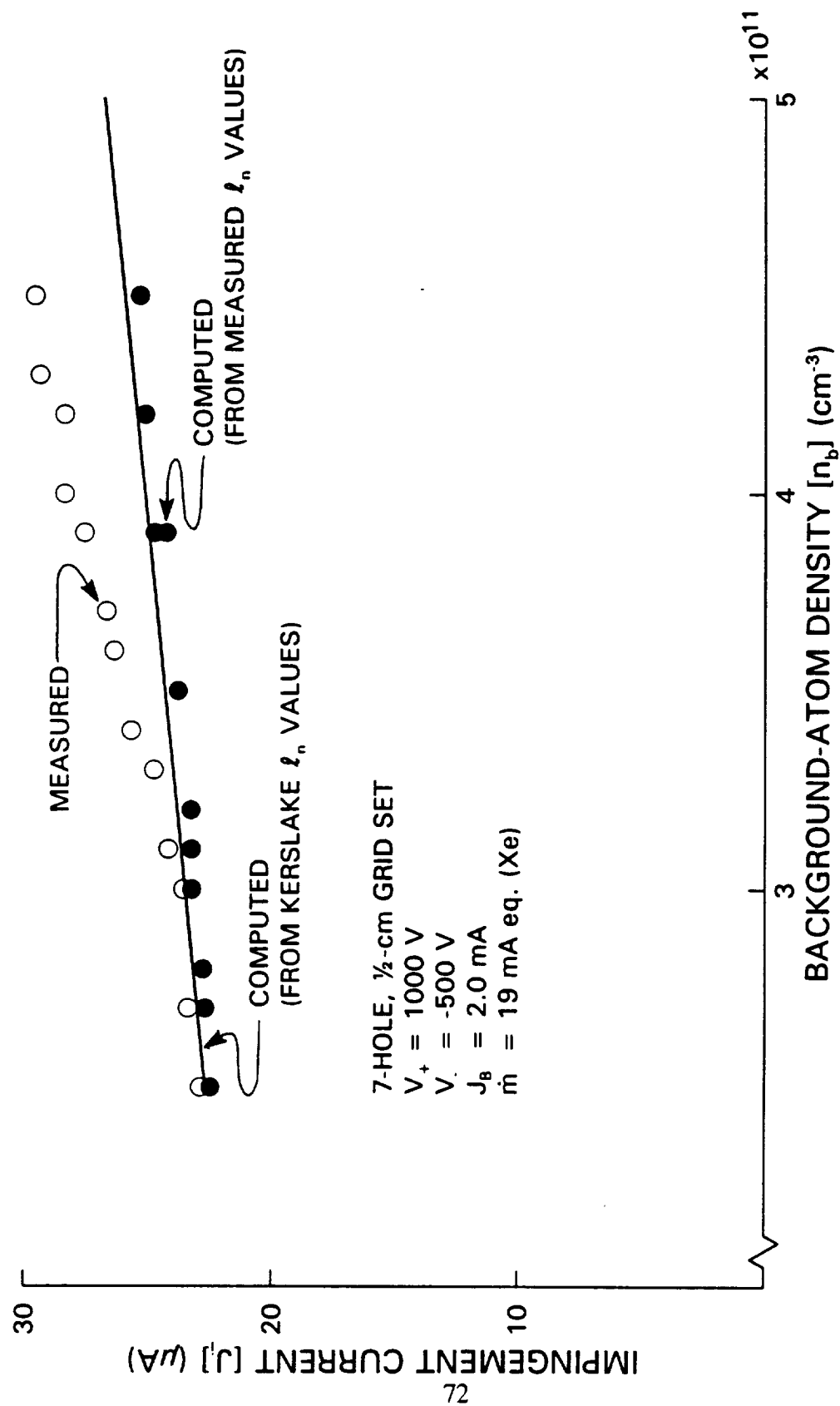


Fig. 27 Effects of Background-Atom Density on Impingement Current for the 7-hole, $\frac{1}{2}$ -cm Grid Set

current-v.-beam-current data obtained using the 7-hole, 1-cm grid set are given on Fig. 28. They show that the measured impingement current increases linearly from 25 to 75 μA as the beam current is increased from 0.75 to 3.0 mA and beyond this direct impingement begins to occur. The impingement-current values computed using the measured ℓ_n data and the Kerslake ℓ_n values show excellent agreement, within 20 to 30%, with the measured-impingement current over the beam current range where direct impingement is not present. A comparison between the two computed impingement currents (solid circles and line) shows agreement that is good. This good agreement in the impingement currents is a consequence of the good agreement between the measured and computed (Kerslake) values for ℓ_n .

The impingement currents of Fig. 29 were obtained as the beam current extracted from the 15-cm SHAG set was varied from 50 to 600 mA and they show that the measured-impingement current increased from 1 to 9 mA over this beam current range. The figure also shows good agreement between the two computed impingement currents and among the measured and two computed currents (within 30% over the beam current range investigated). An interesting observation related to the data of Fig. 29 is that the measured impingement current should vary as $J_b(1 - \eta_u)$ if the source-dominated-impingement current (the first two terms of Eq. 22) is the major component of the impingement current. For the constant \dot{m} condition associated with these data, an increase in beam current from zero to $J_b = \dot{m}$ (an increase in propellant utilization from zero to one) should cause the impingement current to rise from zero to a maximum at $J_b = 370 \text{ mA}$ (at $\eta_u = 1/2$) and then

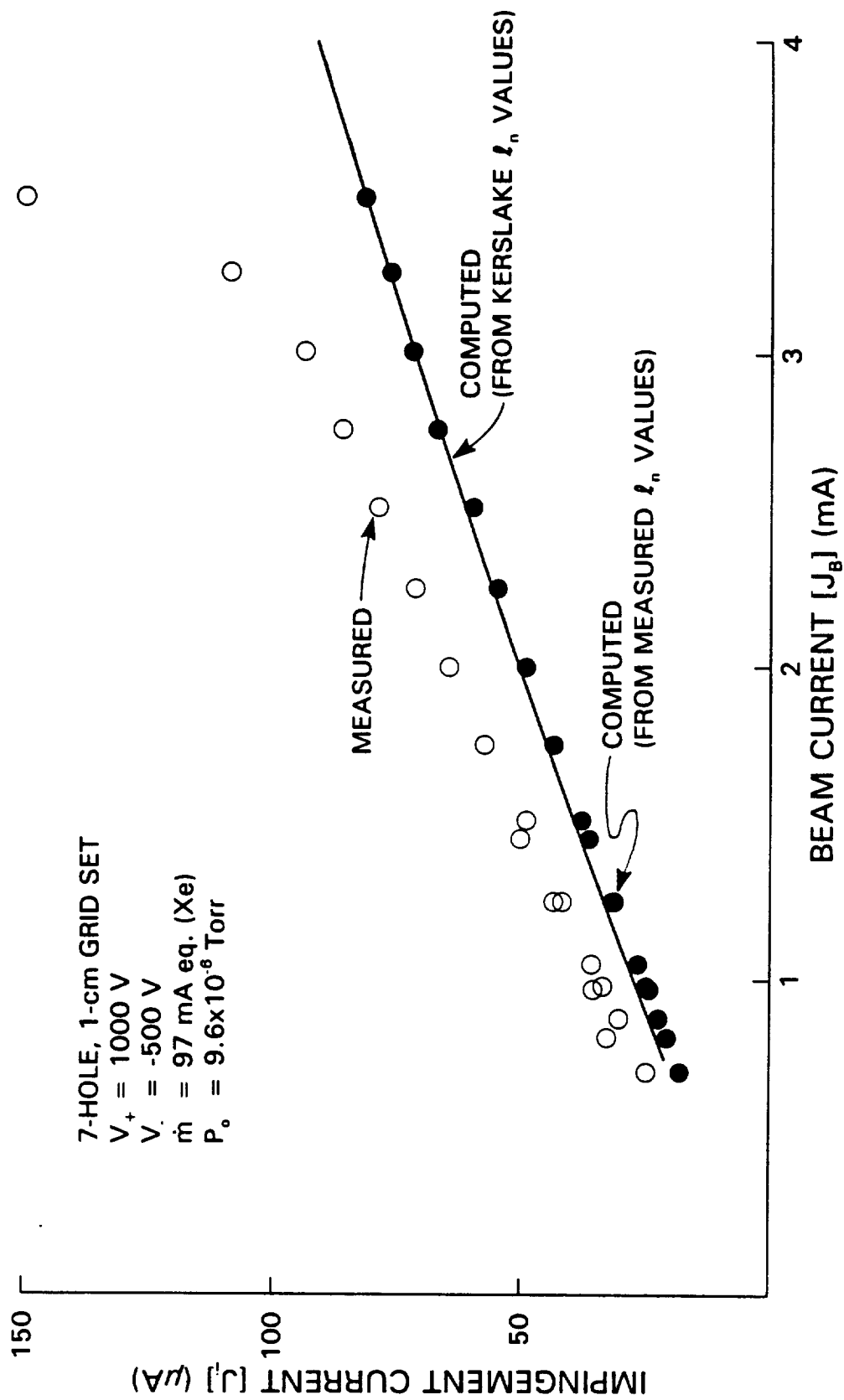


Fig. 28 Effects of Beam Current on Impingement Current for the 7-hole, 1-cm Grid Set

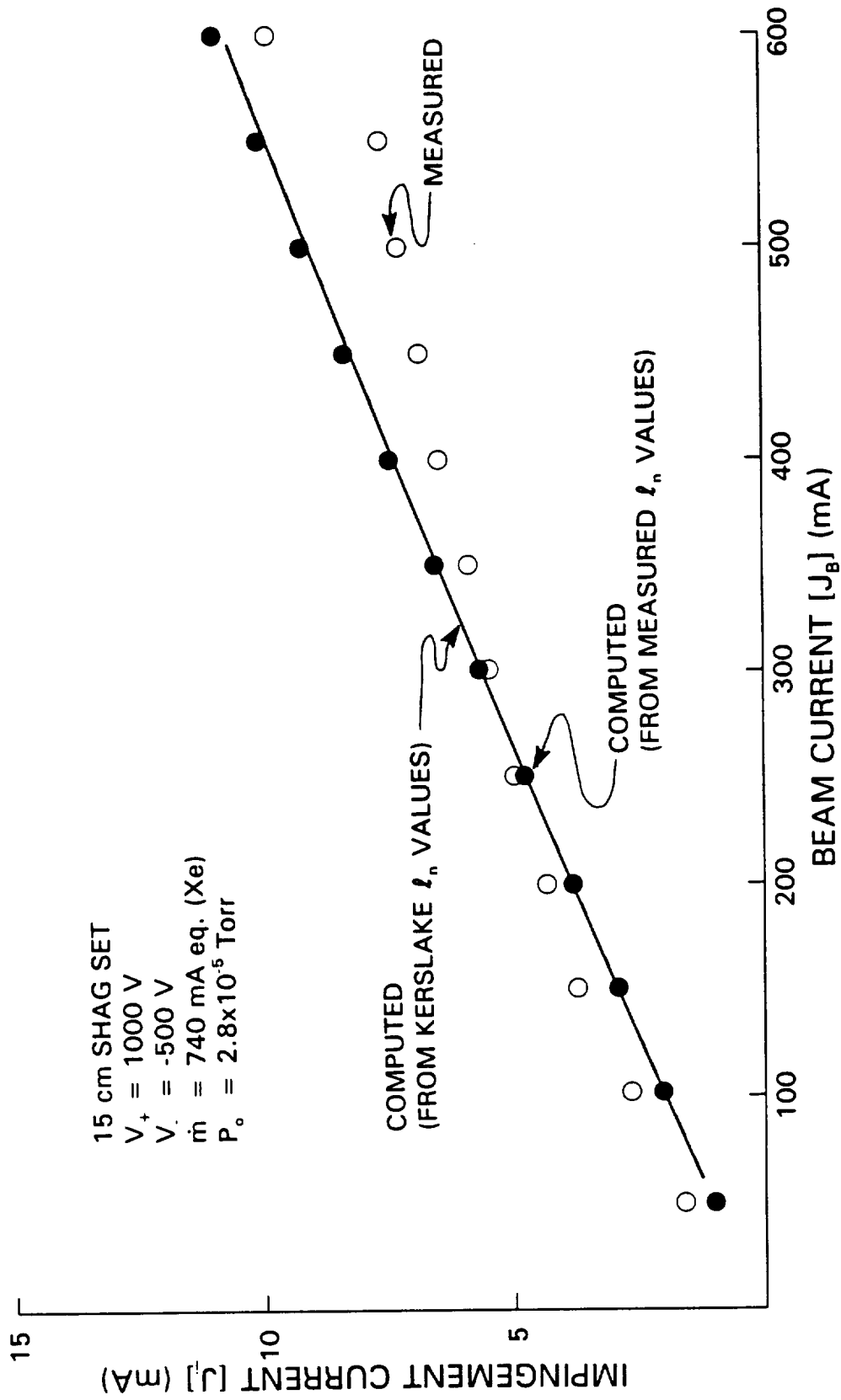


Fig. 29 Effects of Beam Current on Impingement Current for the 15-cm SHAG Set

decrease to zero as J_B approaches 740 mA ($\eta_u \rightarrow 1$). In contrast, if the background-dominated-impingement current (the last term of Eq. 22) is the dominate component, the impingement current should increase linearly with beam current. The linear variation between J_B and J_i (both computed and measured) on Fig. 29 suggests that the background-dominated-impingement current is the major component for SERT II ion thruster equipped with the 15-cm SHAG set. To determine if the background-dominated impingement current is the major component when the 7-hole grid sets are used and the variations in propellant utilization are too small ($1/2$ to 8%) to see this effect, the fractions of the total-impingement current due to both the source- and background-dominated components were calculated using the Kerslake values for ℓ_n (from Fig. 15). The results of these calculations are presented on Fig. 30 and they show that for the 7-hole, $1/2$ -cm-grid set, having an exposed accel-grid diameter of 5.5 cm, approximately 90% of the impingement current is created by charge-exchange collisions between beamlet ions and neutral propellant atoms (i.e., the source term dominated). In contrast, the impingement-current fractions presented on Fig. 31, which were computed for the 15-cm SHAG set having an exposed accel-grid diameter of ~ 15 cm, show that the background-dominated-impingement current is responsible for most of the impingement-current ions. This is consistent with the results of Fig. 29. Thus, the data of Figs. 29-31 indicate that the combination of the larger exposed accel-grid area and higher background pressures associated with the 15-cm-SHAG set causes a fundamental change in the dominate impingement-current component. It is noted that the source-dominated impingement current fraction

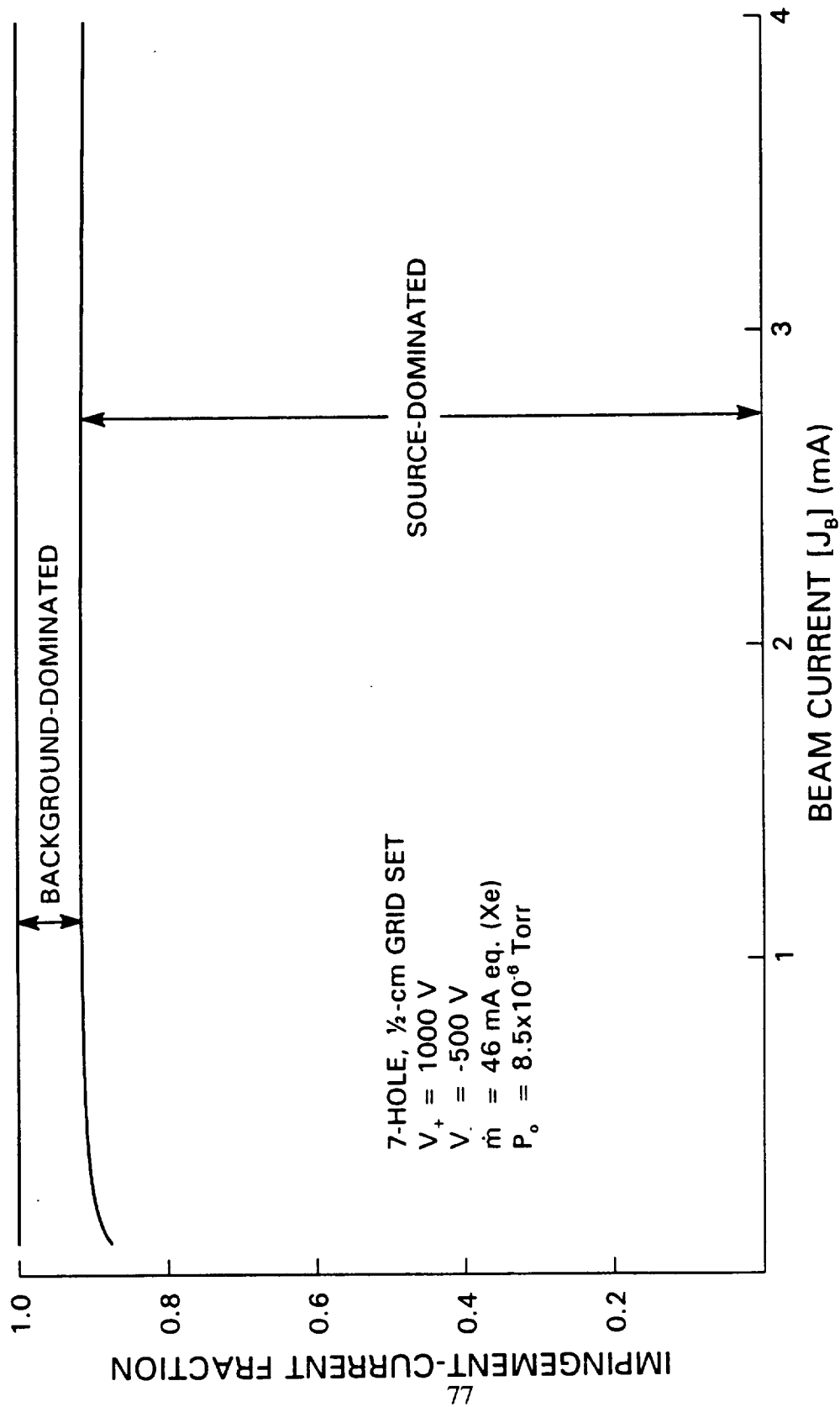


Fig. 30 Effects of Beam Current on the Background- and Source-Dominated-Impingement Current Fractions for the 7-hole, 1/2-cm Grid Set

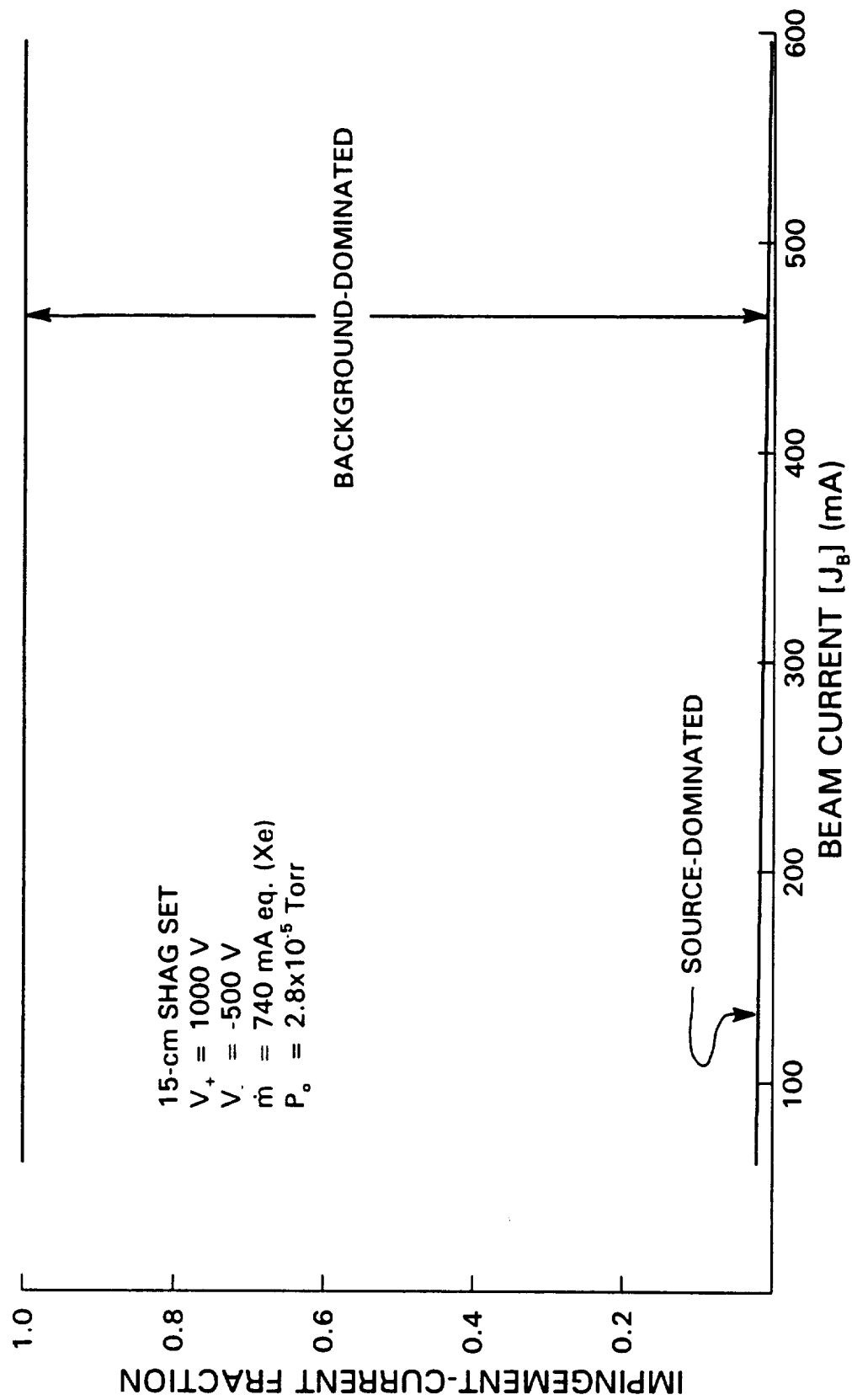


Fig. 31 Effects of Beam Current on the Background- and Source-Dominated-Impingement Current Fractions for the 15-cm SHAG Set

presented on Fig. 31 is considered too low ($< 0.05\%$) because the Monte-Carlo simulation of the propellant flow through this grid set neglects the effects of adjacent apertures. It is expected that more accurate simulations of the propellant flow through the 15-cm-SHAG set should result in impingement-to-beam-current ratios typical of those measured on mercury-ion thrusters (i.e., $\frac{1}{4} - \frac{1}{2}\%$) [31].

V. Conclusions

Experimental data and theoretical calculations presented within this dissertation have shown that ions that impinge on the accel grid cause sputter erosion, and limit thruster lifetimes are produced predominately by charge-exchange collisions and not by single- or multi-step electron-impact ionization. In addition, potential fields measured in the regions downstream of an ion thruster accel grid show that all charge-exchange ions created upstream of a neutralization boundary defined by the neutralization length should impinge on the accel grid. These potential data also show that charge-exchange ions created within the ambient plasma (downstream of the neutralization length) could reach the accel grid because no continuous potential ridge, which would prevent their upstream migration, exists across the ion beam. A simple 1-D model describing the production of charge-exchange ions both upstream and downstream of the neutralization length was developed to reflect these three experimental observations. This model includes two components of the total impingement current, namely, the source-dominated- and the background-dominated-impingement currents. The source-dominated-impingement current is that due to charge-exchange ions created by collisions between beamlet ions and neutral atoms (propellant) that come directly from the thruster and it is, therefore, a direct consequence of the thruster operation and cannot be eliminated. However, the

background-dominated component is due to charge-exchange ions created by collisions between beamlet ions and background atoms present within the vacuum facility. This component is therefore a consequence of the finite, vacuum-facility pumping speed and will not be present in experiments conducted in high-pumping speed facilities or during space operation of ion thrusters.

To compute impingement currents, values for the neutralization length are required. Experimental values for ℓ_n and those calculated using the Kerslake model were shown to agree over a wide range of operating conditions (beam current, grid potentials, background-atom density, neutralizer-bias voltage and keeper current) using three different grid sets. Using both measured and computed neutralization lengths, impingement currents were calculated for the SERT II ion thruster over a wide range of thruster and neutralizer operating condition along with grid set geometries and these currents were generally found to agree with measured values to within $\pm 30\%$. To obtain initial estimates for the impingement current components, simple equations were presented and they showed that the characteristic length for the source-dominated impingement current is the neutralization length while the characteristic length for the background-dominated impingement current is equal to $\frac{1}{4}$ of the exposed accel grid diameter. Furthermore, this 1-D model was used to show that, for the SERT II thruster equipped with the 15-cm-SHAG set the higher-than-expected impingement-to-beam-current ratio (2 to 3% for the data presented) was due to a large background-dominated, impingement-current component. This suggests that if the same tests were conducted in a facility having a high-pumping speed,

impingement-to-beam-current ratios similar to those obtained for mercury thrusters could be obtained. Because charge-exchange cross-sections and masses for mercury and xenon are relatively similar, this suggests, in turn, that xenon-ion thrusters will have lifetimes that are comparable to those of mercury thrusters.

VI. References

1. Brophy, J.R., Pless, L.C., Mueller, J., and Anderson, J.R., "Operating Characteristics of a 15-cm dia. Ion Engine for Small Planetary Spacecraft," IEPC 3-110, 23rd International Electric Propulsion Conference, Seattle, WA, Sept 13-16, 1993.
2. Fearn, D.G., and Hughes, R.C., "The T5 10 cm mercury Ion Thruster," AIAA Paper 78-650, AIAA 13th Electric Propulsion Conference, San Diego, CA, April 1978.
3. Aston, G., "Electric Propulsion: A Far Reaching Technology," AIAA Paper No. 85-2028, 18th International Electric Propulsion Conference, Alexandria, VA., Sept. 30 - Oct. 2, 1985.
4. Atkins, K.L., "Mission Applications of Electric Propulsion," AIAA Paper No. 74-1085, AIAA/SAE 10th Propulsion Conference, San Diego, CA, Oct. 21-23, 1974.
5. Sauer, C., "Application of Solar Electric Propulsion to Future Planetary Missions," AIAA Paper No. 87-1053, 19th International Electric Propulsion Conference, Colorado Springs, CO, May 11-13, 1987.
6. Jones, R.M., "A Comparison of Potential Electric Propulsion Systems for Orbit Transfer," AIAA Paper No. 82-1871, 16th International Electric Propulsion Conference, New Orleans, LA, Nov. 17-19, 1982.
7. Free, B.A., "Economic Tradeoff Studies for Electric Propulsion Missions on Communications Satellites," AIAA Paper No. 71-683, AIAA/SAE 7th Propulsion Joint Specialist Conference, Salt Lake City, UT, June 14-18, 1971.
8. Collett, C.R. et al., "Thruster Endurance Test," NASA CR-135011, May 1976.
9. Dulgeroff, C.R., et al., "Ion Thruster System (8-cm) cyclic Endurance Test," NASA CR-174745, Oct. 1984.

10. Brophy J. and Pless, L., "Test-To-Failure of a Two-Grid, 30-cm dia. Ion Accelerator System," IEPC 93-172, 23rd International Electric Propulsion Conference, Sept. 13-17, 1993, Seattle, WA.
11. Rawlin, V.K., "Erosion Characteristics of Two-grid Ion Accelerating Systems," IEPC 93-175, 23rd International Electric Propulsion Conference, Seattle WA. Sept. 13-16, 1993.
12. Patterson, M.J., and Rawlin, V.K., "Derated Ion Thruster Design Issues," IEPC 91-150, 22nd International Electric Propulsion Conference, Viareggio, Italy, Oct. 14-17, 1991.
13. Rawlin, V.K., "Internal Erosion Rates of a 10-kW Xenon Ion Thruster," AIAA Paper No. 88-2912, 24th Joint Propulsion Conference, Boston, MA, July 11-13, 1988.
14. Kerslake, W.R., "Charge-Exchange Effects on the Accelerator Impingement of an Electron-Bombardment Ion Rocket," NASA TN D-1657, May 1963.
15. Monheiser, J.M., "Advanced Electric Propulsion Research - 1990," NASA CR-187103, May 1991.
16. Chen, F.F, Introduction To Plasma Physics and Controlled Fusion. Vol. 1 Plasma Physics, Plenum Press, New York and London, 1984, p. 157.
17. Rapp, D. and Francis, W.E., "Charge Exchange between Gaseous Ions and Atoms," The Journal of Chemical Physics, Volume 37, No. 11, Dec. 1, 1962, pp. 2631-2645.
18. Squires, L. and Baer, T., "Cross sections for symmetric charge transfer reactions of Xe^+ and NO^+ in selected internal and translational energy states," The Journal of Chemical Physics, Volume 65, No. 10, Nov. 15, 1976, pp. 4001-4006.
19. Hishinuma, N., "Charge Transfer Cross Sections of $^2\text{P}_{3/2}$ and $^2\text{P}_{1/2}$ Xe Ions in Xe and O_2 ," J. Phys. Soc. Japan, Volume 32, 1972, p. 1452.
20. Rapp, D. and Englander-Golden, P., "Total Cross Sections for Ionization and Attachment in Gases by Electron Impact. I. Positive Ionization," Journal of Chemical Physics, Vol. 43, No. 5, Sept. 1, 1965, pp. 1464-1479.
21. Burns, P.J., Loehrke, R.I., Dolaghan, J.S. and Maltby, J.D., "Photon Tracing in Axisymmetric Enclosures," HTD-Vol. 203, Developments in Radiative Heat Transfer, ASME 1992.

22. Kaufman, H.R., "One-Dimensional Analysis of Ion Rockets," NASA TN D-61, March 1960.
23. Anderson, J.R., "The Divergence Characteristics of Constrained-Sheath Optics Systems for use With 5-eV Atomic Oxygen Sources," CR - 182238, Jan. 1989.
24. Wilbur, P. J., Beattie, J. R., and Hyman, J, "Approach to the Parametric Design of Ion Thrusters," Journal of Propulsion and Power, Vol. 6, No. 5, Sept./Oct. 1990, pp. 575-583.
25. Kerslake, W.R., "Development and Flight History of SERT II Spacecraft," NASA TM-105636, July 1992.
26. Williams, J.D., "An Experimental Investigation of Hollow Cathode-Based Plasma Contactors," NASA CR-187120, May 1991, pp. 91-107.
27. Hershkowitz, N., "How Langmuir Probes Work," Appears in Plasma Diagnostics: Discharge Parameters and Chemistry, O. Auciello, O. and D. Flamm, ed., Vol. 1, Academic Press, Inc., San Diego CA, 1989, pp. 113-183.
28. Smith, J.R., Hershkowitz, N., Coakley, P., "Inflection-Point Method of Interpreting Emissive Probe Characteristics," Rev. Sci. Instrum. Vol. 50, No. 2, Feb. 1979, pp. 210-218.
29. "Product and Vacuum Technology Reference Book", Leybold-Heraeus Inc., 1993, pp. 48-55.
30. Patterson, M.J. and Verhey, T.R., "5-kW Xenon Ion Thruster Lifetest," AIAA Paper 90-2543, 21st International Electric Propulsion Conference, Orlando, FL, July 18-20, 1990.
31. Kami, S., Dulgeroff, C., and Bechtel, R.T., "Status of the J-Series 30-cm Mercury Ion Thruster," AIAA-82-1904, 16th International Electric Propulsion Conference, Nov. 17-19, 1982, New Orleans, LA.

VII. Appendix A: Interpretation of Hot-Filament-Emissive Probe Floating Potential Data Obtained Within an Ion Beamlet

Several techniques have been developed to measure potentials of plasmas having densities ranging from zero to 10^{12} cm^{-3} [24,25,26]. The simplest method involves measuring the potential at which a hot-filament emissive probe floats when it is placed within the plasma. This floating potential is defined as the probe potential required to assure a zero net current to the probe. To understand why a hot-filament emissive probe floats near plasma potential consider the hypothetical emissive-probe-filament surface pictured on Fig. A1. This figure shows the probe surface submersed within an ambient plasma (a zero-net-charge-density region) and connected to a reference potential (typically ground) through a high impedance voltmeter (depicted here as an ideal voltmeter and a known input impedance). First, consider the case where the probe surface is not heated to thermionic emission temperatures (i.e., a cold-filament). Because the mass difference between ions and electrons causes the current of electrons toward the probe to be much greater than the current of ions, the probe must charge negative of plasma potential so electron collection will be retarded and ion collection will be enhanced. Consequently, a cold-filament emissive probe will float negative of plasma potential.

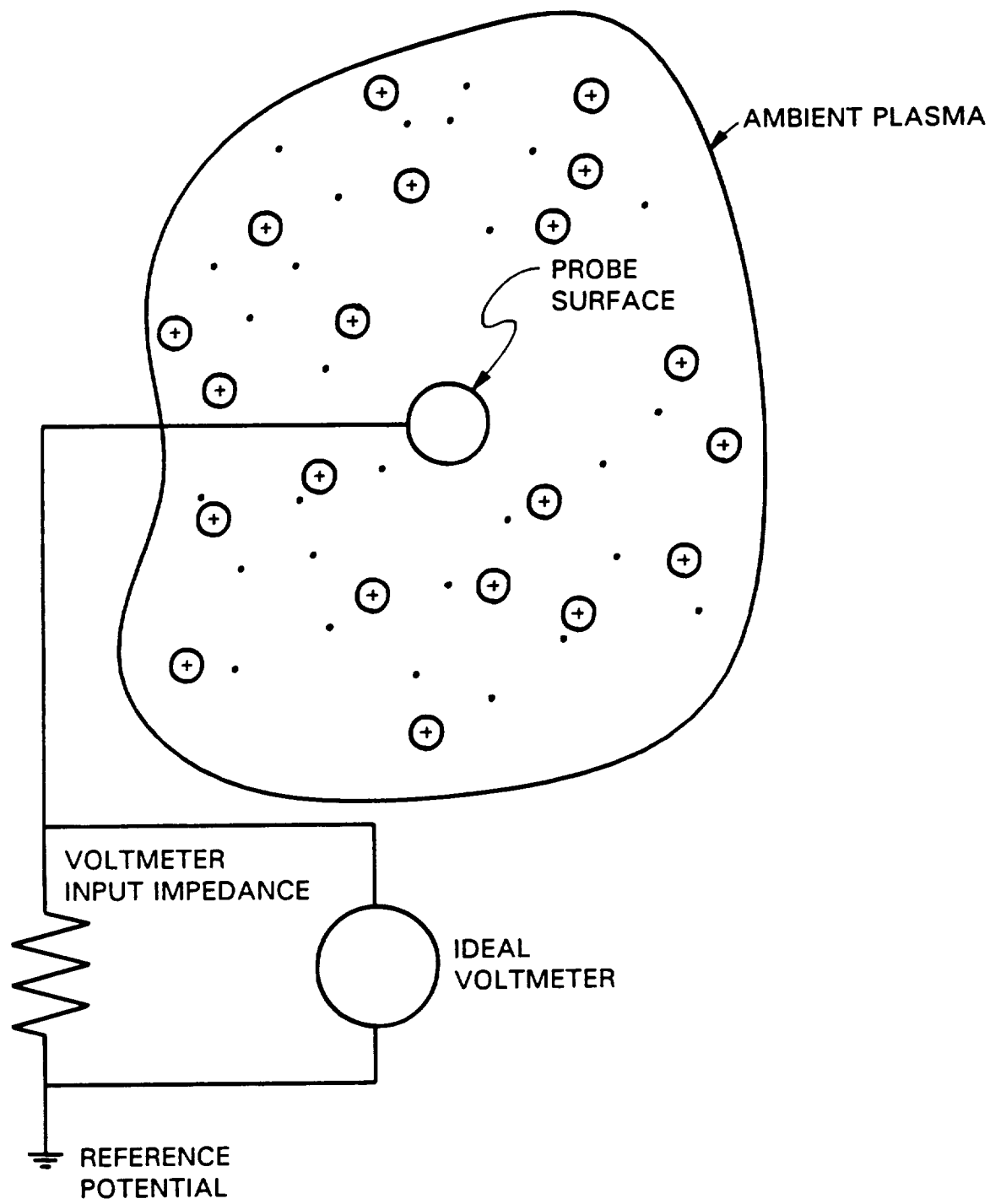


Fig. A1 A Hypothetical Probe Surface Submerged in an Ambient Plasma

Heating of the probe filament reduces the difference between the probe floating potential and plasma potential because it enables electron emission from the probe surface and this compensates for some of the electron collection. This emission reduces the negative charge of the probe surface and allows it to float close to plasma potential. For example, when the probe potential is negative of plasma potential it will emit electrons thereby increasing its potential and if the probe potential is greater than plasma potential it will stop emitting and begin to collect electrons from the ambient plasma thereby reducing its potential. This competing effect of electron emission and collection allows a hot-filament-emissive probe to float very near plasma potential. Because of its simplicity, hot-filament emissive probes are commonly used to measure the potentials in plasmas having densities greater than 10^8 cm^{-3} [26]. The presence of the voltmeter should have no affect on the plasma potential as long as the input impedance of the voltmeter is sufficiently large so the current drawn does not perturb the plasma density.

In contrast to the typical laboratory plasmas described above, regions downstream of ion thrusters generate an ion beamlet flowing through both an ambient plasma region that contains ions and electrons and a positive-charge density region near the accel grid that contains only ions. Probing in the vicinity of this ion beamlet yields emissive-probe-floating-potential data more complex and more difficult to interpret than those measured in a plasma. Consider the situation presented on Fig. A2, which again shows a hypothetical probe surface this time immersed in an ambient plasma through which an ion beamlet is flowing. Similar to the processes

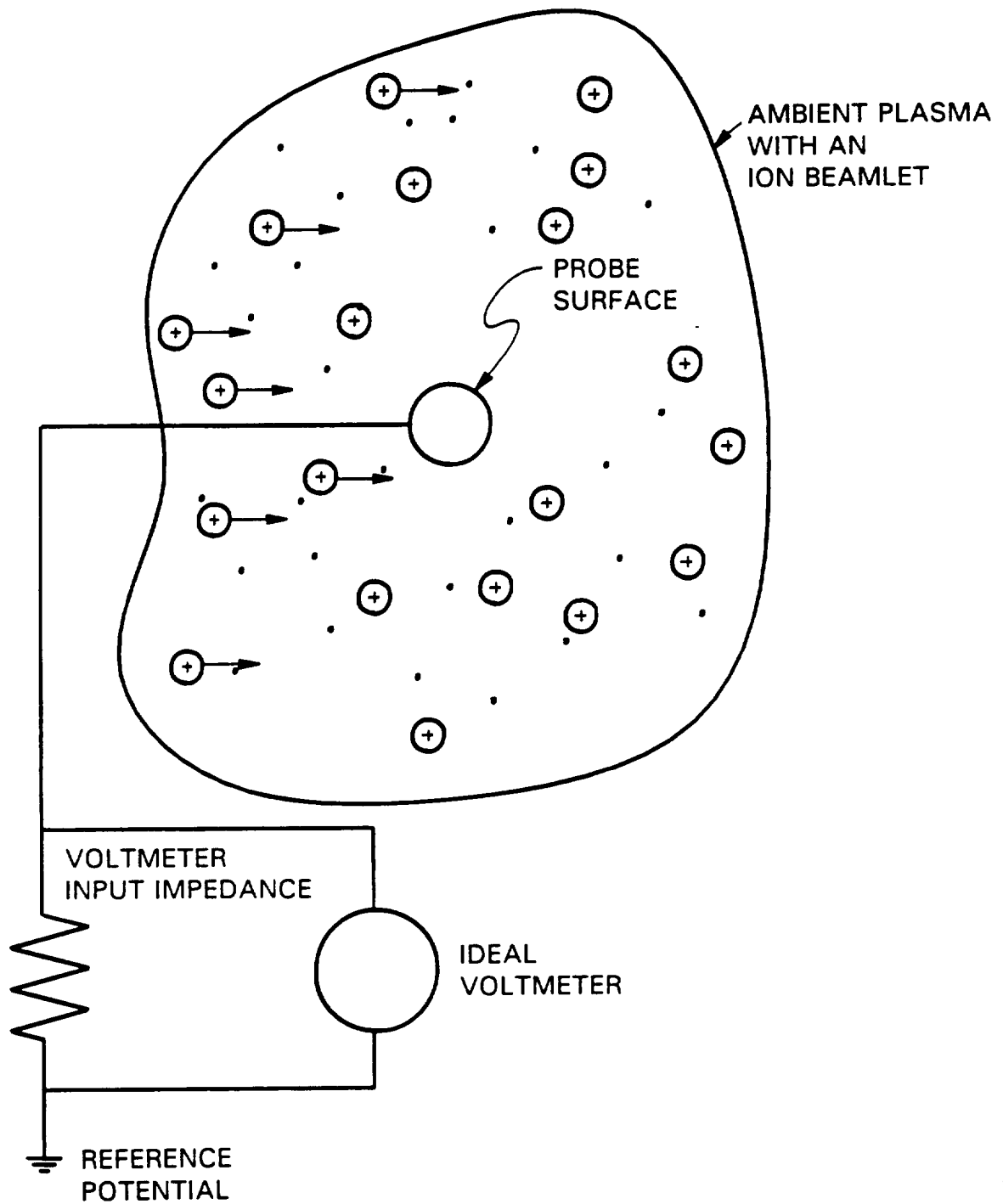


Fig. A2 A Hypothetical Probe Surface Submerged in an Ambient Plasma with an Ion Beamlet

described above, the competition between electron collection and emission at the probe causes the hot-filament-floating potential to be near plasma potential. The dominate effect induced by the presence of the ion beamlet is that it increases the ion current to the probe thereby reducing the electron emission current required to cause the probe to float at plasma potential. Therefore, a hot-filament emissive probe in an ambient plasma through which an ion beamlet is flowing should still float at the local potential. Again, the presence of the voltmeter should have a negligible effect on the measurement of plasma potential provided the input impedance of the voltmeter is large enough to prevent the current drawn from influencing the plasma density.

To understand how the absence of the ambient plasma affects the floating potential it is helpful to consider Fig. A3. This figure shows a probe surface connected to a reference potential through a high-impedance voltmeter and immersed in an ion beamlet. In the absence of ambient plasma electrons, the probe surface cannot collect negative charge and the only way for the positive charge associated with the beamlet ions to escape the probe is through the voltmeter (with its associated impedance) to reference potential. Hence, the reference potential and the voltmeter impedance can affect the potential at which the probe floats. To understand how they effect the floating potential consider the case where the local potential is negative of the reference potential. Since no electrons are present in the surrounding environment to charge the probe negative, in the absence of an ion current, the probe would float at the reference potential independent of the local potential. Since the floating potential is greater than the local potential, electron emission will not occur and ion

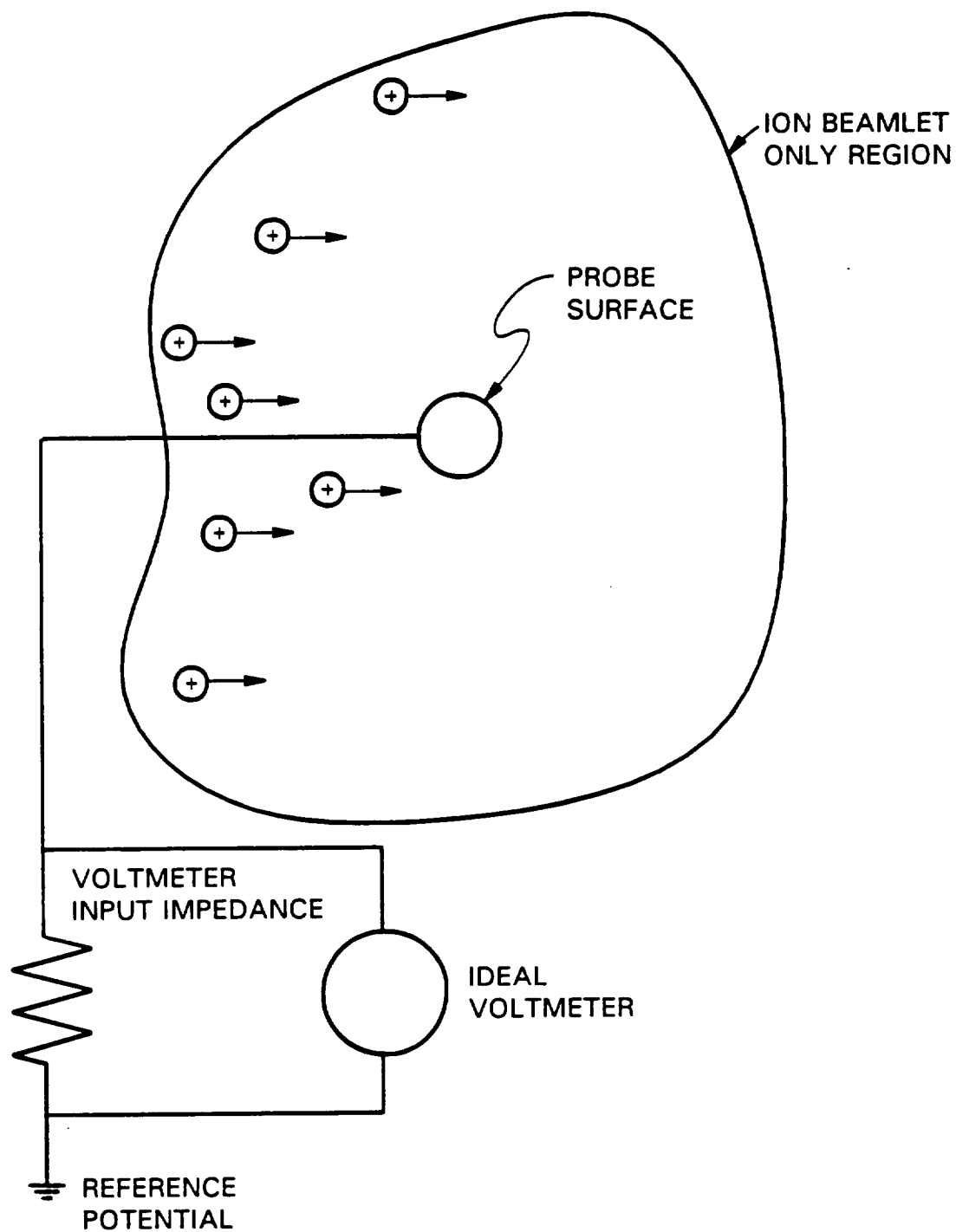


Fig. A3 A Hypothetical Probe Surface Submerged in an Ion Beamlet

collection causes the potential of the probe to increase above the reference by an amount equal to the product of the ion current collected by the probe and the voltmeter input impedance. Thus a hot-filament-emissive probe will always indicate an erroneously high potential when its reference potential is too great. Next, consider the case where the local potential is greater than reference potential. In this case the probe collects ions and a hot, emissive filament can emit electrons. Both of these effects will cause the probe potential to increase and approach the true potential of the environment. The probe electron-emission-current will be approximately equal to the local potential divided by the voltmeter-impedance, hence if the impedance is too small the probe will be required to emit a very large current. This discussion suggests that a hot-filament emissive probe operating within an ion beamlet will accurately follow variations in the local potential provided the reference potential is sufficiently negative.

To demonstrate the effects induced by ion beamlets, consider the data traces presented on Fig. A4. These data were obtained on the thruster centerline using the grid set identified on and operated at the conditions given on the figure legend. The solid line shows the floating potential measured using a hot-filament probe referenced to ground, while the circular points are the floating potentials measured when the probe was referenced to -500 V. The figure shows that within the ambient plasma (downstream of 0.75 cm) both data sets measure a constant potential of 4 V independent of the probe reference. Between 0.25 and 0.75 cm, however, the solid line shows that indeed when the probe is referenced to ground the minimum

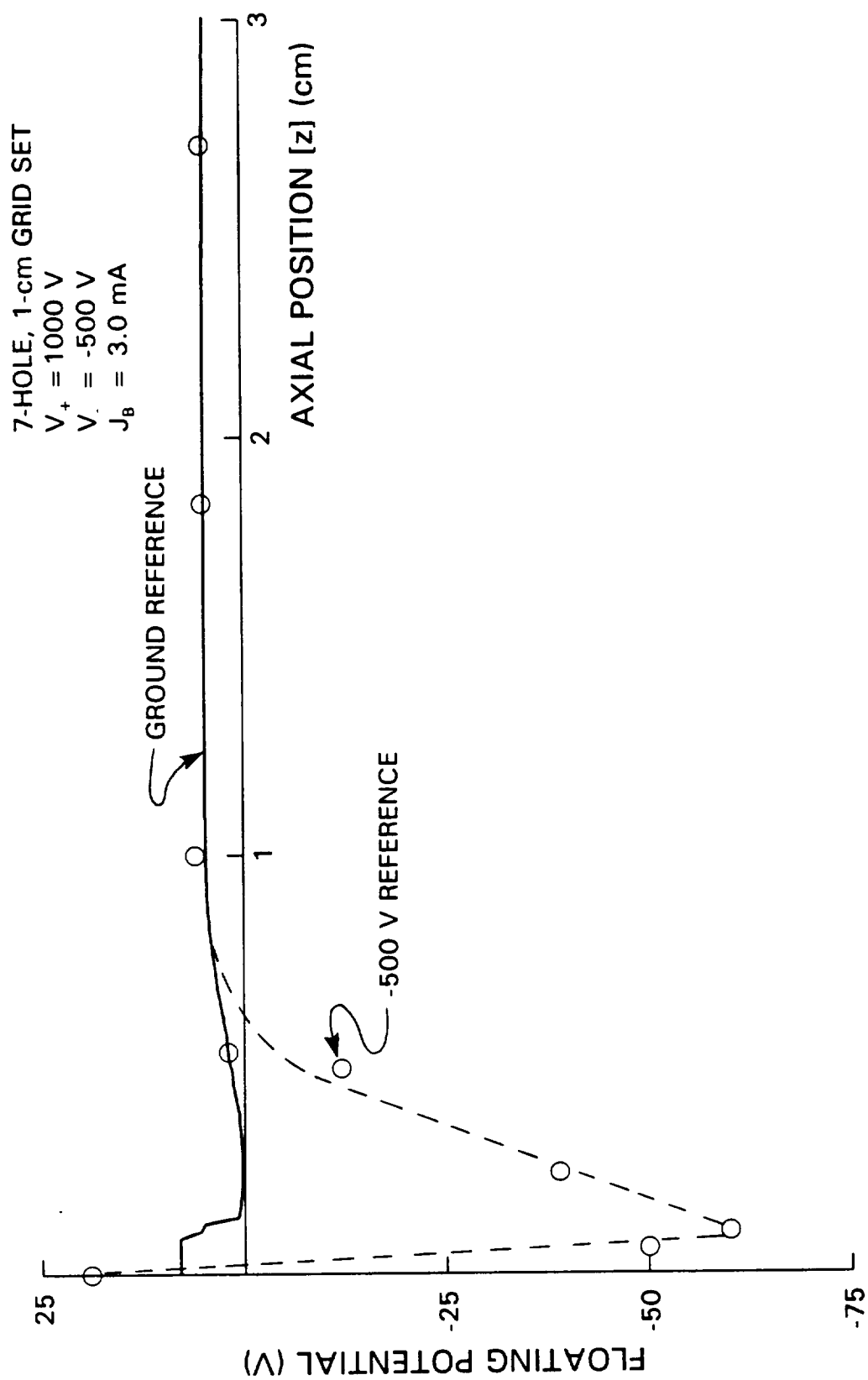


Fig. A4 Effects of the Reference Potential on the Hot-Filament, Emissive-Probe, Floating Potential

measurable potential is ground while the circles show that for a -500 V reference the probe will float at negative potentials as expected. Lastly, upstream of 0.25 cm both data sets indicate potentials greater than ground. These positive potentials near the accel grid are believed to be caused by the finite size of the probe hot-filament (~ 3 mm) and the steep potential gradients (present in the region between the screen and accel grids). These effects cause the probe filament to float somewhere between the screen and accel grid potentials and it is believed that if a smaller filament could be constructed, potential data similar to the hypothetical plot of Fig. 2b could be measured.